Development of New Red Phosphors and Effects of Coordination Environment around Activator on Luminescence Properties

新規赤色蛍光体の開発と賦活剤周りの配位環境に由来する発光特性への影響

Akihiro NAKANISHI

Department of Chemical Science and Technology
Graduate School of Advanced Technology and Science
Tokushima University

March, 2024

Contents

Chapter 1

Introduction

1.1 White-light LEDs

After the discovery of blue light emitting diode (LED) based on high-quality crystals of GaN, AlGaN, and GaInN in the early 1990s [1,2], the development of white solid-state lighting with blue, green, and red LEDs was accelerated. However, the degradation rate of these LEDs was different, causing variations in white color lighting. In addition, the color rendering index was poor due to the narrow-band-emitting of the three primary colors. Therefore, it was proposed that the combination of a blue LED and a broad-band yellow phosphor could produce better white light. These phosphor-converted LEDs (pcLEDs) have been widely used in lighting applications and social life. In the 2010s, the cost and supply of rare earth, which is used for activators for phosphors, had programs due to China's export controls. The development of new phosphors without rare earth as an activator has been rapidly conducted in terms of cost and supply. There are some properties required of phosphors for the pcLEDs;

・conversion from blue to other colors, such as red, yellow, and green.

・single phosphor white (a blue LED and a yellow phosphor), or Multi-phosphor white (a UV LED and blue, green, and red phosphors).

・thermal stability, ideally it will be stable to at least 200 °C.

There are four approaches to realizing the white light from the pcLEDs. It is difficult to obtain white light LEDs with both a high color rendering index and luminous efficacy due to trade-off.

(a) A combination of blue, green, and red LEDs, poor color rendering index, and highest luminous efficacy in (a)~(d).

(b) A pcLED consisting of a blue LED and green and red phosphors, a higher color rendering index but lower luminous efficacy than that of (a).

(c) A pcLED consisting of a blue LED and a yellow-orange phosphor, lower color rendering index but higher luminous efficacy than that of (b)

(d) A pcLED consisting of a UV LED and blue, green, and red phosphors, highest color rendering index but lowest luminous efficacy in (a)~(d).

It is important to generate the white light to match the requirements of users. High color rendering of white light is necessary for a commercial or domestic situation, while the color rendering is not so important to read a book with only black and white pages. Color rendering index above 80% is acceptable for domestic use. The discovery of new green and red phosphors is the most important challenge for lighting and display applications [3].

1.2 Phosphors for pcLEDs

1.2.1 Metal-oxide based phosphor

Some advantages of oxide-based phosphor are good chemical stability and simple synthetic method compared with other anion-based phosphor.

1.2.1.1 Yttrium Aluminum Garnet Activated by Trivalent Cerium ($Y_3Al_5O_{12}$: Ce^{3+})

The first report of $Y_3Al_5O_{12}$: Ce^{3+} (YAG: Ce^{3+}) was in 1967, this material was used for a cathodoluminescence phosphor [4]. A combination of blue LED and YAG: Ce^{3+} generates white light with low cost and high luminous efficacy.

The excitation and emission peak of YAG: Ce^{3+} is at around 470 nm and 550 nm, respectively. The emission wavelength is modulated by the element doping such as Gd^{3+} and Ga^{3+} to the A-site or B-site of the host material of YAG [5-7]. In summary, the YAG: Ce^{3+} is applied to generate white light with high luminous efficacy under blue light excitation, and its emission is controlled by element substitution. However, the other phosphors are necessary to obtain a high color rendering index.

1.2.1.2 Alkaline earth metal silicates

Barry reported Eu^{2+}-activated $An_3MgSi_2O_8$ (An = Ca^{2+}, Sr^{2+}, and Ba^{2+}) phosphors with high luminous efficacy. The emission wavelength is controlled by changing alkaline earth metal ions in this system [8]. Eu^{2+}-activated An_2SiO_4 (An = Ca^{2+}, Sr^{2+}, and Ba^{2+}) phosphors were also reported as green to yellow phosphors for pcLEDs. The cationic size of alkaline earth metal affects the emission wavelength [9-12]. These phosphors were commercialized, but they have poor stability. The luminescence properties depend on the condition of their synthesis:

・suitable row materials (purity, reactivity)

・selection of good flux materials

・reducing atmosphere (N_2/H_2)

・heating temperature and rate of heating (and cooling)

1.2.2 Metal-nitride based phosphor

There are some advantages of nitrides over oxides:

・highly condensed anionic networks, resulting in high density, good chemical stability, and greater hardness.

・large red-shift, small thermal quenching.

1.2.2.1 β-sialon: Eu

β-sialon is one of the best green phosphors for LED backlight because of its narrow emission and high thermal stability. The crystal structure of β-sialon is derived from β-Si_3N_4, with the solid solution of $Si_{6-z}Al_zO_zN_{8-z}$ ($0 < z \leq 4.2$) [13]. Hirosaki et al. first reported the luminescence property of Eu^{2+}-activated β-sialon, which is synthesized by calcination of powder mixture of Si_3N_4, AlN, and Al_2O_3 and Eu_2O_3 at 1900-2100 °C in a 1.0 MPa N_2 atmosphere [14]. The phosphor exhibits the green emission at 535 nm with the FWHM of 55 nm under blue light excitation of 450 nm.

1.2.2.2 Ca-α-sialon: Eu

The crystal structure of Ca-α-sialon is derived from α-Si_3N_4, with the solid solution of $Ca_{m/2}Si_{12-m-n}Al_{m+n}O_nN_{16-n}$ (Ca is the modifier, and charge neutral is adjusted by the value of m) [15]. Eu^{2+}-activated Ca-α-sialon exhibits the yellow emission at 582 nm with the FWHM of 94 nm under UV or blue light excitation with a very low thermal quenching (The luminescence intensity decreases by 10% at 150 °C).

1.2.2.3 $CaAlSiN_3$: Eu

Eu^{2+}-activated $CaAlSiN_3$ exhibits red emission at 658 nm with the FWHM of 94 nm. The excitation band is also broad, and it has a small thermal quenching as well as the Eu^{2+}-activated Ca-α-sialon. The emission band is modulated by replacing Ca with Sr. The emission peak is blue-shifted from 650 nm to 610 nm by increasing the amount of Sr [16].

1.3 Host materials for phosphors

The luminescence properties are greatly affected by the coordination environment around the activator in the host lattice. The coordination environment depends on the crystal structure of host materials. The polyhedron with different coordination numbers (such as tetrahedron, octahedron, dodecahedron, tetradecahedron, etc.) constitutes the various crystal structures. Here, the perovskite-, pyrochlore-, and garnet-type structures are focused in this study. Ideally, the crystal system of these structures is cubic. The polyhedron that constitutes these crystal structures is different. The structural properties are discussed next.

1.3.1 Perovskite-type structure

The general formula of the perovskite-type structure is ABX_3: twelve-coordinated tetradecahedral site (AX_{12}), six-coordinated octahedral site (BX_6), and X-site. Cations with various valence states occupy the A- and B-sites, while anions occupy the X-site in the perovskite-type structure. The crystal structure of the perovskite-type structure is shown in Fig. 1.1 [17].

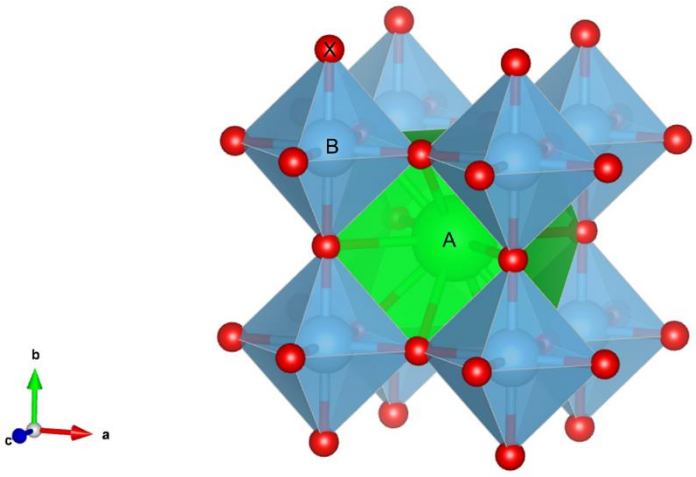

Fig.1.1 Crystal structure of the perovskite.

The Goldschmidt tolerance factor (t) describes the stabilization region of perovskites. It is written by only ionic radius: R_A (twelve-coordinate radius), R_B (six-coordinate radius), and R_X as shown below;

$$t = \frac{R_A + R_X}{\sqrt{2}(R_B + R_X)}$$

Goldschmidt suggested that the perovskite-type structure would form when the value of t is close to 1. Despite its simple equation, the tolerance factor predicts the structural properties, especially for oxides. Ideally, when the value of t is 1, the crystal system of perovskites is cubic. If the range of t is 0.9-1, a cubic perovskite would form. If the value of t is greater than 1, a hexagonal packing of the AX_3 layers is preferred. In the case that the value of t is within 0.71-0.9, the symmetry of the crystal system would be lower due to the distortion of BX_6 octahedra tilting. The structure-field map has been proposed as shown in Fig. 1.2. The stabilization area of perovskites is obtained by the tolerance factor and the octahedral factor (R_B/R_X) [18].

Cation ordering at the A- or B-site in the perovskite-type structure would affect properties such as ferroelectricity and piezoelectricity [19]. In the case of the double perovskite of $A_2BB'X_6$, an ordered arrangement would be present if the valence state difference between B and B' is greater than two such as $Sr^{2+}{}_2Ni^{2+}W^{6+}O_6$. Differences in the cation radius and/or bonding preference also affect the arrangement. The displacement of the B-site cation is caused by the arrangement or deficiency of the A-site cation. In compounds such as $La_{1/3}NbO_3$, $La_{1/3}TaO_3$, and $Nd_{1/3}NbO_3$, cation layers of the lanthanoid and deficiency are arranged alternatively, resulting in the displacement of the B-site cation to the A-site layer with lower positive charge as shown in Fig. 1.3.

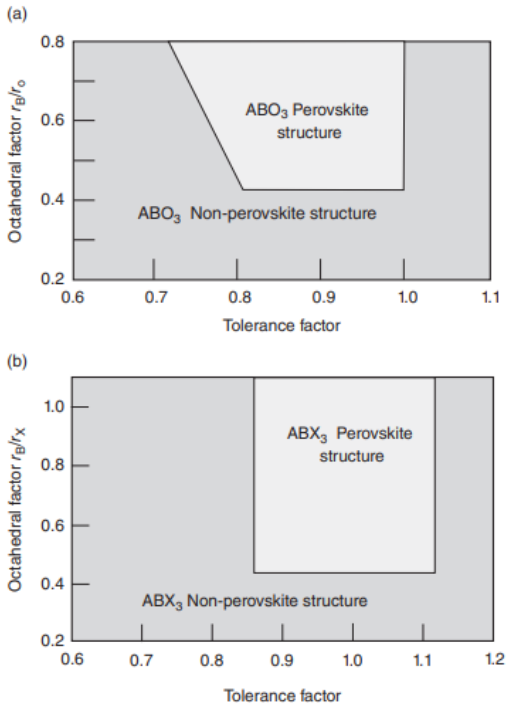

Fig.1.2 Structure-field maps, schematic; tolerance factor t versus octahedral factor: (a) oxides; (b) halides [18].

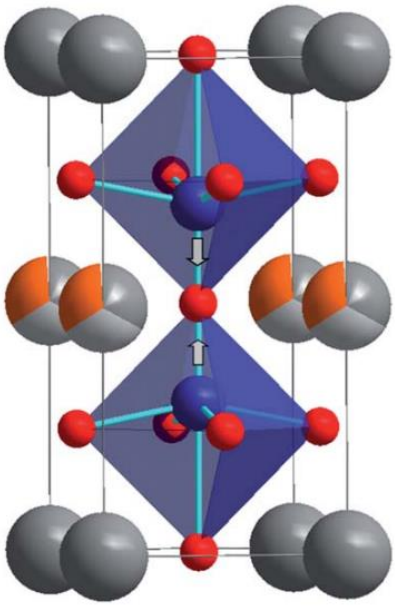

Fig.1.3 The crystal structure of the $Li_{3x}R_{2/3-x}TiO_3$ perovskites. The color scheme is blue (Ti^{4+}), red (O^{2-}), and grey (R^{3+}). The large three-colored spheres are randomly occupied by R^{3+}, Li^{+}, and vacancies. The arrows show the displacements of the Ti^{4+} ions towards the anions in the layer containing the vacancies [19].

1.3.2 Pyrochlore-type structure

The general formula of the pyrochlore-type structure is $A_2B_2X_6Y$: eight-coordinated site (AX_6Y_2), six-coordinated octahedral site (BX_6), and X-site. Cations with various valence states occupy the A- and B-sites, while anions occupy the X- and Y-site in the pyrochlore-type structure (usually A is a divalent or trivalent cation and B is a transition metal). The crystal structure of the pyrochlore-type structure is shown in Fig. 1.4. The crystal system of the pyrochlore-type structure is cubic with a space group of Fd-3m (No. 227) and unit cell with Z = 8. The pyrochlore-type structure consists of two polyhedra: eight-coordinated dodecahedral (Wyckoff position: 16d, fractional coordinate (0, 0, 0)); six-coordinated octahedral sites (Wyckoff position: 16c, fractional coordinate (1/2, 1/2, 1/2)). There are two Wyckoff positions of oxygen: 8b, fractional coordinate (1/4, 1/4, 1/4), and 48 f, fractional coordinate (x, 1/4, 1/4). There is only one adjustable fractional coordinate *x* for the X atom. *x* is usually in the range from 0.320 to 0.345 [20].

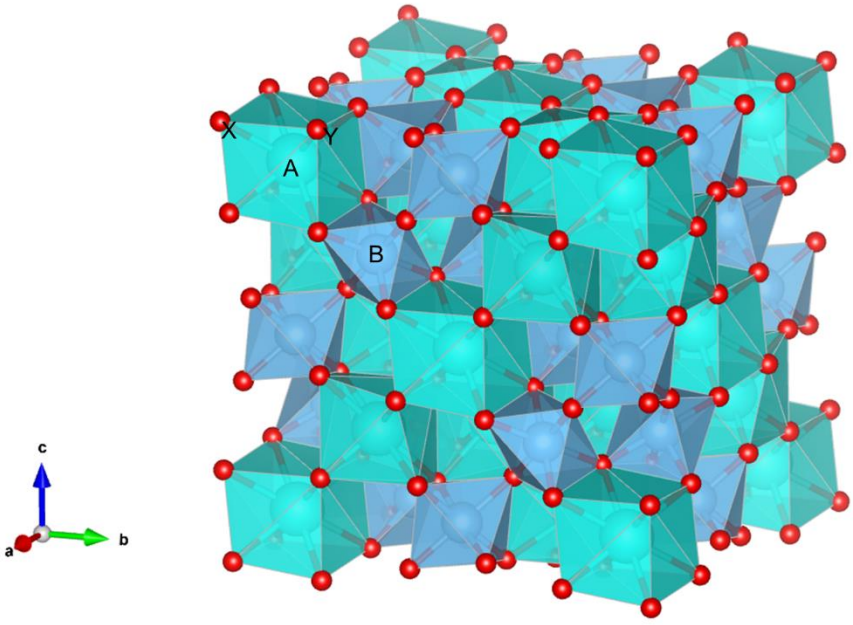

Fig. 1.4 Crystal structure of the pyrochlore.

1.3.3 Garnet-type structure

The general formula of the garnet-type structure is $A_3B_2C_3X_{12}$: eight-coordinated dodecahedral site (AX_8), six-coordinated octahedral site (BX_6), four-coordinated tetrahedral site (CX_4), and X-site. Cations with various valence states occupy the A- and B-sites, while anions occupy the X-site in the garnet-type structure. The crystal structure of the garnet-type structure is shown in Fig. 1.5. The crystal system of the garnet-type structure is cubic with a space group of Ia-3d (No. 230) and unit cell with Z = 8. The garnet-type structure consists of three polyhedra: eight-coordinated dodecahedral (Wyckoff position: 24c, fractional cooordinate (1/8, 0, 1/4)); six-coordinated octahedral (Wyckoff position: 16a, fractional coordinate (0, 0, 0)); and four-coordinated tetrahedral sites (Wyckoff position: 24d, fractional coordinate (3/8, 0, 1/4)). The Wyckoff position and fractional coordinate of oxygen are 96 h and (x, y, z), respectively. The fractional coordinates of A-, B-, and C-site are fixed, and that of X-site is adjustable [21].

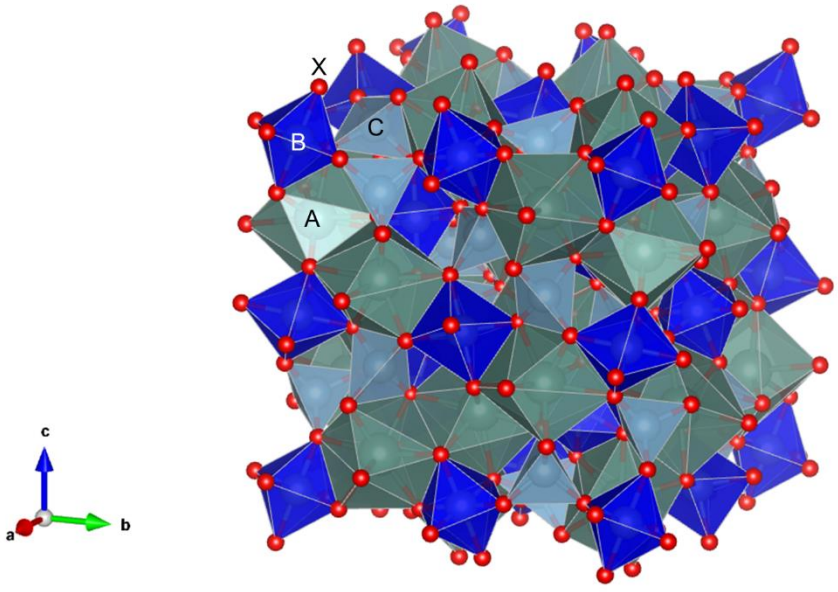

Fig. 1.5 Crystal structure of the garnet.

Song et al. have proposed the tolerance factor of the garnet-type structure [22]. It is written by only ionic radius as well as that of perovskite:

$$\tau = \frac{3\sqrt{(R_B + R_X)^2 - \frac{4}{9}(R_A + R_X)^2}}{2(R_C + R_X)}$$

The value of the tolerance factor is in the range from 0.748 to 1.333. The garnet-type $Ca_3Al_2Si_3O_{12}$ is within the range, while $Sr_3Al_2Si_3O_{12}$ and $Ba_3Al_2Si_3O_{12}$ (τ = 0.690 and 0.391) are not reported. This is because the ionic radius of Sr^{2+} and Ba^{2+} is larger than that of Ca^{2+}, resulting in the difficulty of connection between polyhedra.

1.4 Luminescence mechanism of phosphor

When a material is exposed to radiation such as UV light, X-ray, or electron beam, electrons are excited from ground states to excited states. After relaxation, the excited electrons fall to the ground states, and the excited energy is released as light; This phenomenon is called “Luminescence”. The difference between the energy of excitation and emission is called “Stokes shift”. Phosphor is a material that shows the luminescence. Fig. 1.6 shows the luminescence mechanism, including excitation of radiation, thermal relaxation, and emission.

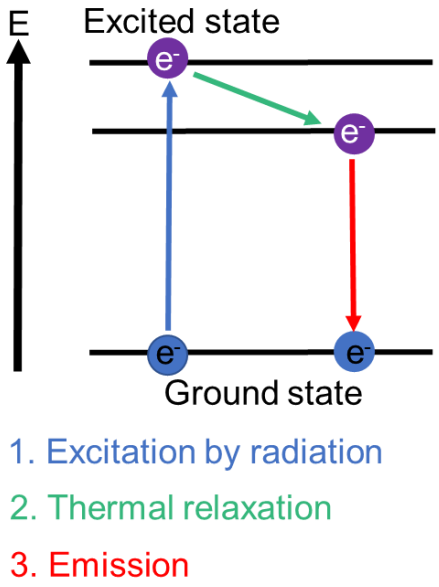

Fig. 1.6 The luminescence mechanism, including excitation of radiation, thermal relaxation, and emission.

Inorganic phosphor consists of an activator and host material. In general, small amounts of activators for the host material (0.5%~1%) are better to optimize the luminescence property. There are some types of transitions and activators [23]:

1. 1s↔2p transition (ex. F (fluoride))
2. ns^2↔ns, np transition (ex. Tl^+-type ion, Ga^+, In^+, Tl^+, Ge^{2+}, Sn^{2+}, Pb^{2+}, Sb^{3+}, Bi^{3+}, Cu^-, Ag^-, Au^-)
3. d↔d transition (ex. Transition metal ions)
4. f↔f transition (ex. Lanthanide and actinide ions)
5. 4f↔4f, 5d transition (ex. Ce^{3+}, Sm^{2+}, Eu^{2+}, Tm^{2+}, Yb^{2+}, Pr^{3+}, Tb^{3+})
6. Charge transfer transition

The configurational coordinate model is utilized to understand the luminescence mechanism in detail as shown in Fig. 1.7. The effect of thermal vibration is considered during luminescence phenomena. Franck-Condon principle elucidates the electric transition of luminescence; the displacement of the atom would not occur during the electric transition. After the excitation of electrons, the atoms in the crystal are displaced from the initial position to the equilibrium position, which means the distance between atoms would be longer. This principle implies the electronic transition occurs much faster than the time required for the nucleus to rearrange into a new configuration [24].

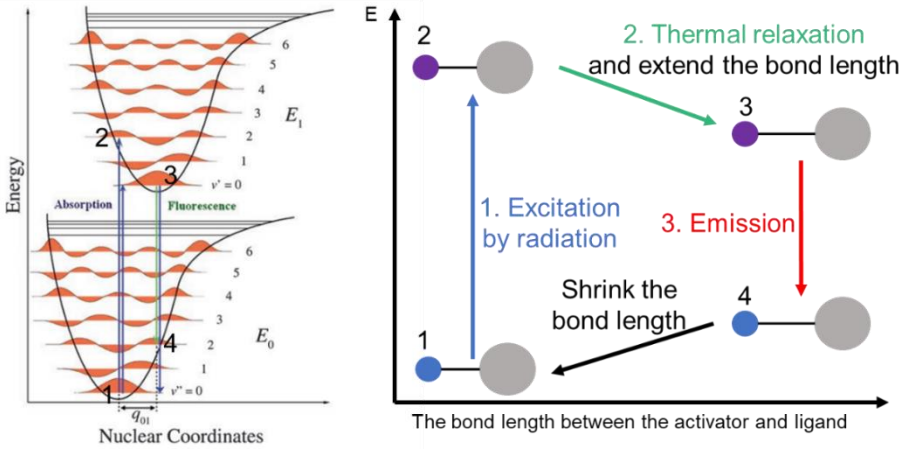

Fig. 1.7 The configurational coordinate model for understanding the luminescence.

1.5 Crystal field theory

The energy levels of elements are discrete and represented by quantum numbers: principle quantum number, orbital angular momentum quantum number (or azimuthal quantum number), magnetic quantum number, and spin magnetic quantum number. Quantum number and orbital angular momentum quantum number are mainly used to represent the energy levels and orbital shape.

When ions are incorporated into liquids or solids, the energy levels are changed from those of gaseous-free ions. Crystal field theory describes these changes, which assumes anions (ligands) surrounding the metal ion as a point electric charge. Crystal field is the interaction between anions (ligands) and the central metal ion. In short, the electric repulsion between anions (negative point charges) and the orbital of metal ions is related to the change in energy level. This theory provides us with the luminescence mechanism of phosphors in which the 3d transition metal ions are used as activators [25].

When the 3d metal ion is incorporated into the six-coordinated site as shown in Fig. 1.8, these anions (ligands) affect the energy levels of the 3d orbital. The fivefold degenerate 3d orbitals split into triply degenerate orbitals (t_{2g} orbital) and doubly degenerate orbitals (e_g orbital). The energy difference between t_{2g} and e_g orbital is 10Dq. The crystal field splitting depends on the coordination environment in a crystal. The crystal field splitting for regular tetrahedron, octahedron, cube, and cuboctahedron were calculated to be 40Dq/9, 90Dq/9, 80Dq/9, and 45Dq/9 [26] as shown in Fig. 1.9. Absorption and emission spectra of metal ions greatly depend on the degree of crystal field.

In the case of metal ions with d^2~d^8, not only the crystal field splitting but also electric repulsion between electrons is considered. The electric repulsion between

electrons is described by the Racah parameter (A, B, and C). These parameters also describe the spectral term. Tanabe and Sugano elucidated the electron configuration interaction for the d^2 to d^8 configuration in an octahedral crystal field, which is called the Tanabe-Sugano diagram. The vertical and horizontal axis of the diagram is the energy level and crystal field splitting standardized by the Racah parameter B. Fig. 1.10 shows the Tanabe-Sugano diagram for the d^3 configuration in an octahedral crystal field. In the case of Cr^{3+} and Mn^{4+} with the d^3 configuration, the transitions from the ground level $^4A_2$ (t_2^3) to $^4T_2$ (t_2^2e) and $^4T_1$ (t_2^2e) are observed in the excitation spectra. After the non-radiation transition from the excited states to the energy level ^2E_g, the transition from ^2E_g (t_2^3) to $^4A_2$ (t_2^3) is observed in the emission spectra. The emission wavelength from Mn^{4+} is not affected by the crystal field (Dq/B) so much, because the ground state of $^4A_2$ and excited state of ^2E are nearly parallel for Dq/B in the diagram [25].

The Tanabe-Sugano diagram is used to analyze the crystal field splitting with three parameters: Dq, B, and C. However, it is not possible to determine the splitting with this diagram when an activator is at the lower symmetry than cubic. The crystal field parameters (CFPs) are useful to describe the crystal field Hamiltonian around an activator. The Hamiltonian of the crystal field is represented as [27]:

$$\mathcal{H} = \sum_{k,q} B_q^k \, C_q^k$$

where B_q^k are the CFPs that have all the structural and geometrical information about the host matrix, and C_q^k are components of tensor operators. The number k must be even; it takes values of 0, 2, 4, and 6 for 4f electrons. The point group restricts the values for q. In the case of lanthanoid ions with f-orbital, the crystal field also affects the energy levels

of f-orbital, depending on the symmetry around the metal-ion site.

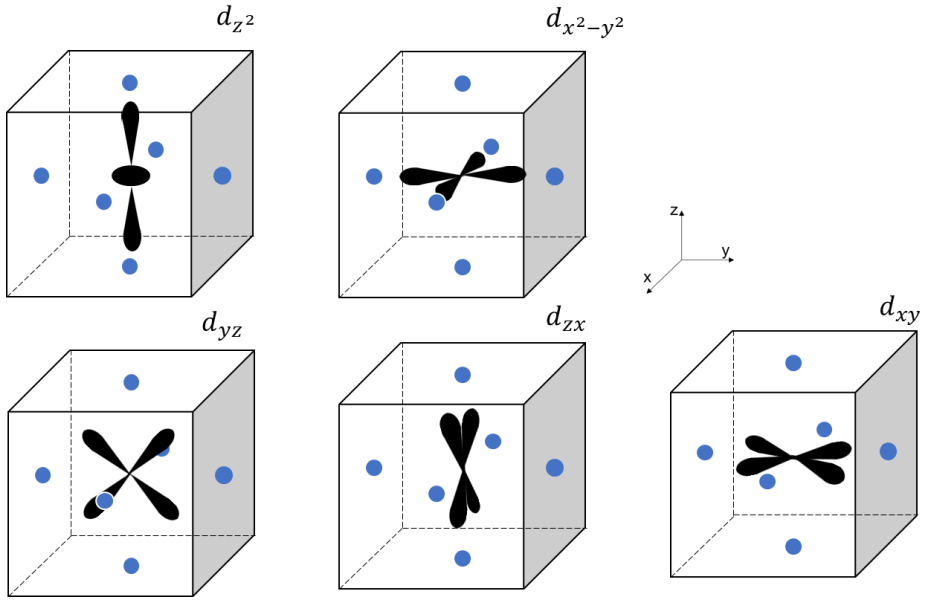

Fig.1.8 The d-orbitals surrounded by ligands (negative charges) at the six-coordinated site.

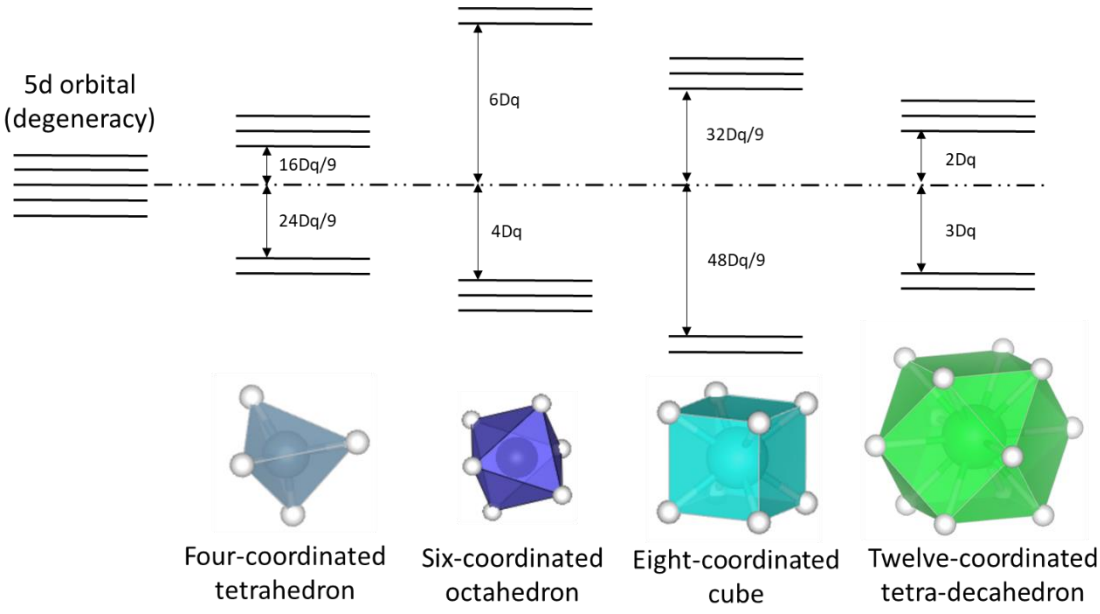

Fig.1.9 Crystal-field splitting of d-orbital in various polyhedral potentials. The dashed line represents the 5-fold unsplit energy levels [26].

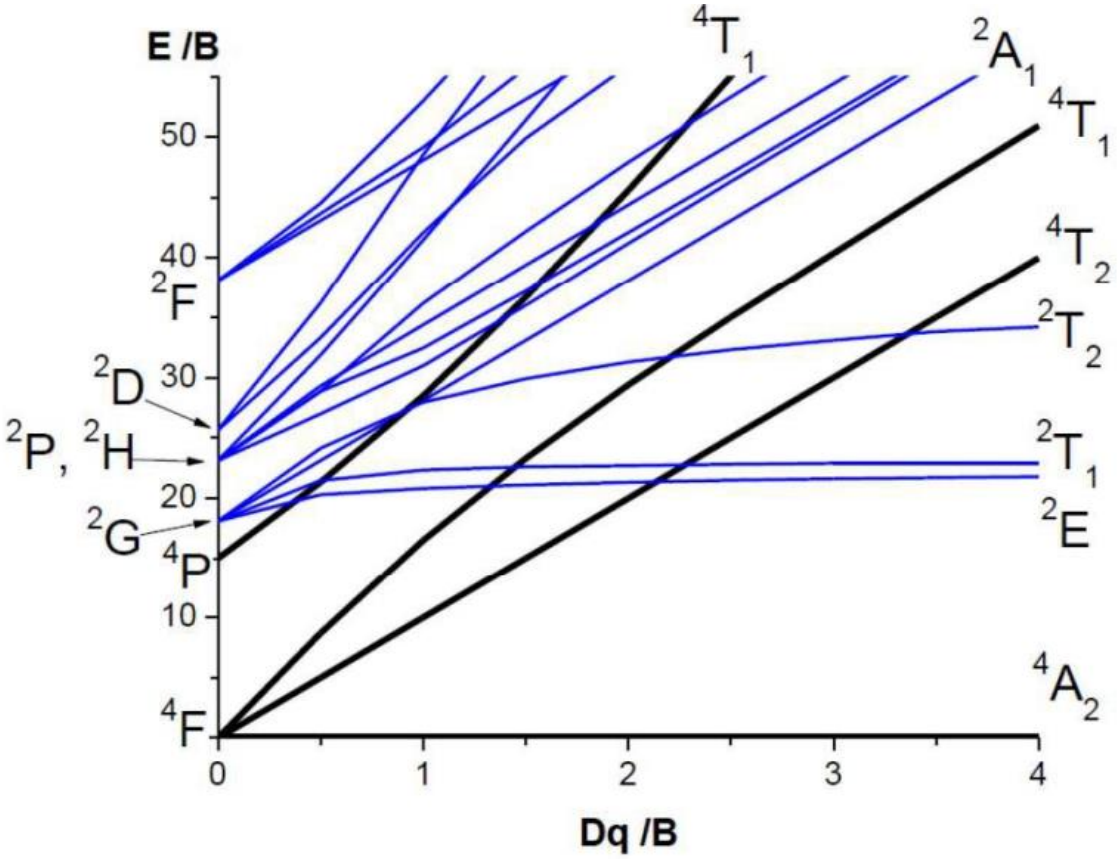

Fig.1.10 Tanabe-Sugano diagram for the d3 electron configuration in the octahedral crystal field.

1.6 Induced electric dipole transition: Judd-Ofelt theory

There are three types of electronic transition of lanthanoid ions: 4f-4f transition, 4f-5d transitions, and charge-transfer transitions (metal-to-ligand). Laporte's parity selection rule describes the allowed and forbidden transitions, which implies the transitions between the ground and excited state with the same parity are forbidden, such as d-d or f-f transitions. When the lanthanoid ions are affected by the crystal field (doped into the crystal lattice), non-centrosymmetric interactions allow the mixture of electronic state with opposite parity into the 4f-orbitals, resulting in the partial relaxation of the selection rule, which is called an induced (or forced) electric dipole transition. For Eu^{3+}-activated phosphors, $^5D_0 \rightarrow {}^7F_2$ (~610 nm), $^5D_0 \rightarrow {}^7F_4$ (~710 nm), and $^5D_0 \rightarrow {}^7F_6$ (~810 nm) are the induced electric dipole transitions, while $^5D_0 \rightarrow {}^7F_1$ (~570 nm) is the magnetic dipole transition.

Judd-Ofelt theory is based on the crystal-field concept and produces a simple model for intensities of f-f transitions in solids and solutions [28]. The transition strength P_{ed} is represented with the Judd-Ofelt parameters:

$$P_{ed} = C\left\{\Omega_2\left\|U^{(2)}\right\|^2 + \Omega_4\left\|U^{(4)}\right\|^2 + \Omega_6\left\|U^{(6)}\right\|^2\right\}$$

$$C = \frac{64\pi^4 e^2 v_4^3}{3h(2J+1)}\left[\frac{n(n^2+2)^2}{9}\right]$$

where e is the charge of an electron, n is the refractive index, v is the emission peak wavenumber, h is the Planck constant, and J is the total angular momentum quantum number of the initial energy level $^5D_0$. $\left\|U^{(J)}\right\|^2$ denote the reduced matrix elements from the initial to the excited state, which have an intrinsic value. Ω_2, Ω_4, and Ω_6 are Judd-

Ofelt intensity parameters. The Judd-Ofelt parameters depend on the coordination environment (chemical bonding or site symmetry) around lanthanide ions, especially the excitation and emission spectra of Eu^{3+} are often utilized for the probe of the crystallographic sites [29].

1.7 Purpose of this study

White light LEDs are widely used in social life. However, due to the lack of the red component, the white light LED has a poor color rendering index. To solve this program, some red phosphors, which have the absorption band in the near-UV to blue light, have been synthesized.

Some nitride phosphors have been commercialized because of their good photoluminescence (PL) properties and high stability. The search for new nitride phosphors is still active for further improvement. However, higher temperature (1800-2000 °C) and the reductive atmosphere are needed to synthesize nitrides and sometimes special equipment for high nitrogen pressure is necessary. In the case of oxide phosphors, new oxide phosphors have been developed, taking advantage of low fabrication costs. The achievement of this study is the development of new red phosphors with lower fabrication costs compared with the fabrication of nitride phosphors. In addition, the relationship between PL properties and the coordination environment is revealed. The PL properties depend on the coordination environment around the activator, which is derived from the crystal structure of the host material. Therefore, the oxide host materials were carefully selected in this study. Eu^{3+} and Mn^{4+} were used as activators because they absorb UV and blue light and emit red light, having the possibility of applying to the high-color-rendering white LEDs.

In Chapter 2, the relationship between PL properties and the coordination environment around Eu^{3+} in the garnet-type $Ca_2EuZr_{2-x}Sn_xGa_3O_{12}$ (x = 0, 0.5, 1, 1.5, and 2) phosphors are discussed. There were few reports to investigate the influence of structural distortion on the PL property of Eu^{3+}. The distortion of the eight-coordinated dodecahedron affects the intensity derived from $^5D_0 \rightarrow {}^7F_2$ (~610 nm) and $^5D_0 \rightarrow {}^7F_4$ (~710

nm) transitions of Eu^{3+}. The degree of this distortion was revealed by Rietveld analysis. The Rietveld analysis is an effective way to elucidate the distortion of the eight-coordinated dodecahedron of these phosphors, where Eu^{3+} constitutes the host material of the garnet, because of a diffraction method that describes the average structure of the materials. The coordination environment around Eu^{3+} was described by calculating the edge lengths of the eight-coordinated dodecahedron. A method to describe the rotation angles of the top and bottom faces of the eight-coordinated dodecahedron in a garnet-type structure is proposed by simple geometric calculations utilizing the ratios of the edges of the dodecahedron. This method reveals the relationship between the emission intensity of Eu^{3+} at 610 nm and 710 nm and the coordination environment in the garnet-type structure. Controlling the emission wavelengths is useful for further applications. Phosphors emitting red light near 600 nm have good visibility and are suitable for application in high-color-rendering white LEDs. The infrared wavelength near 700 nm is suitable for plant growth.

In Chapter 3, Mn-activated perovskite-type $La_{5/3}MgTaO_6$ red phosphor and pyrochlore-type Mg_2LaTaO_6 green phosphor are discussed. The Mn-activated perovskite-type $La_{5/3}MgTaO_6$ red phosphors are cost-effective compared with Eu^{3+}-activated phosphors in chapter 2 because Mn is cheaper than Eu. X-ray absorption fine structure (XAFS) spectroscopy methods were utilized to reveal the distortion of the Mn^{4+}-occupied octahedron. It appears that the Rietveld analysis, which was utilized in the previous chapter, reveals the distortion of the polyhedron. However, it is difficult to investigate the coordination environment around only Mn by the Rietveld analysis due to the two points: the analytical methods for describing long-range-order structure (average structure) and low concentration of Mn^{4+} in the host material. It should be noted that the XAFS method

provides important information of the local structure around a specific element [30]. Therefore, it is probable that the XAFS method is suitable for accurately describing the coordination environment around Mn^{4+}. A-site deficiency in the perovskite-type structure plays a crucial role in the red emission of Mn^{4+} in the host material of $La_{5/3}MgTaO_6$ because of the displacement of Mn^{4+}. And also, Mn-activated pyrochlore-type Mg_2LaTaO_6 phosphor exhibited green emission under UV excitation at 254 nm owing to the oxide ion deficiency of Mg_2LaTaO_6, indicating that the defects affect the coordination environment around Mn^{2+} as an activator. In general, the green emission is derived from Mn^{2+}. However, Mn^{2+} is achieved by the calcination in the reductive atmosphere due to lower valence state than Mn^{4+}. The green emission from Mn^{2+} was realized in the crystal structure of the pyrochlore-type Mg_2LaTaO_6 even by the calcination in air atmosphere, resulting in the cost-effective fabrication.

References

[1] H. Amano, M. Kito, K. Hiramatsu et al., *Jpn. J. Appl. Phys*. **28** (1989) L2112-14.

[2] S. Strite, M.E. Lin, H. Morkoc, *Thin Solid Films* **231** (1993) 197-210.

[3] J. Silver, G.R. Fern, R. Withnall, "Color Conversion Phosphors for Light Emitting Diodes", Chapter 3, pp. 91-93 (2017), Wiley.

[4] G. Blasse, A. Brill, *Appl. Phys. Lett.* **11** (2) (1967) 53-5.

[5] J. Silver, Phosphors for LEDs, current state of the air, programs, and needs. Invited lecture, The Future of LEDs, June 26-27 (2006) London.

[6] J.M. Robertson, M.W. van Tol, W.H. Smits, *Philips J. Res.* **36** (1) (1981) 15-30.

[7] W. Rossner, Phosphor Global Summit, Scottsdale, AR, USA, Conference Paper 14 pp.1-18 (2003).

[8] T.L. Barry, *J. Electrochem. Soc.* **115** (1968) 733-8.

[9] J. Meyer, Novel garnet phosphors for LEDs, Phosphor Global Summit, San Diego, CA, USA, Conference Paper 9, pp. 1-13 (2006).

[10] L.M. Levinson, A.M. Srivastava, US Pat. 6429583, Nov. 30 (1998).

[11] K. Ota, A. Hirano, A. Ota et al., US Pat. 6943380, Dec. 28 (2000).

[12] S. Tasch, P. Pacher, G. Roth et al., US Pat. 6809347, Dec. 22 (2003).

[13] K.H. Jack, W.I. Wilson, *Nature Phys. Sci.* **238** (1972) 28-29.

[14] N. Hirosaki, R.-J. Xie, K. Kimoto, *Appl. Phys. Lett.* **86** (2005) 211905.

[15] G.Z. Gao, R. Metselaar, *Chem Mater.* **3** (1991) 242-252.

[16] H. Watanabe, H. Yamane, N. Kijima, *J. Solid State Chem.* **181** (2008) 1848-1852.

[17] J.D. Richard, Perovskites: Structure–Property Relationships Tilley: Wiley (2016).

[18] C. Li, X. Lu, W. Ding, L. Feng, Y. Gao, Z. Guo, *Acta Crystallogr B.* **64** (2008) 702-7.

[19] G. King, P.M. Woodward, *J. Mater. Chem.* **20** (2010) 5785–5796.

[20] M.V. Talanov, V.M. Talanov, Chem. Mater. 33 (2021) 2706−2725.

[21] S. Geller, Crystal chemistry of the garnets, *Z. Kristallogr.* **125** (1967) 1–47.

[22] Z. Song, D. Zhou, Q. Liu, *Acta Cryst.* **C76** (2020) 311.

[23] 蛍光体同学会編　「蛍光体ハンドブック」(1987)

[24] S. Wu et al., "Long Afterglow Phosphorescent Materials", Published by Springer Nature, (2017).

[25] W.M. Yen, S. Shionoya, H. Yamamoto, Phosphor Handbook Second Edition (2006).

[26] S. Zheg, L. Quan-lin, *Chinese Journal of Luminescence* **43** (9) (2022) 1428.

[27] Q. Zhou, L. Dolgov, et al., *J. Mater. Chem.* **C6** (2018) 2652.

[28] JC.G. Bünzli, S.V. Eliseeva, Basics of Lanthanide Photophysics. Ed. P. Hänninen,

and H. Härmä, Vol. 7, pp. 1-45 (2010), Springer.

[29] 足立吟也監修「希土類の材料技術ハンドブック」(2008)

[30] 吉朝朗「回折法と X 線吸収分光（XAFS）法を用いた地球惑星物質の精密構造解析」岩石鉱物科学 **42** (2013) 111-122.

Chapter 2

Emission modulation of Eu^{3+} via symmetry around dodecahedron in garnet-type $Ca_2EuZr_{2-x}Sn_xGa_3O_{12}$ (x = 0, 0.5, 1, 1.5, and 2) phosphors

2.1 Introduction

White LEDs have applications in numerous fields owing to their high energy efficiency and long lifetime [1-3]. White LEDs are developed via a combination of blue LEDs [4] and yellow phosphor ($Y_3Al_5O_{12}:Ce^{3+}$), wherein white light is created based on the three primary colors of light [5]. However, realizing the full spectrum of sunlight in white LEDs is difficult due to the lack of red components [6]. To address this problem, red phosphors, which are excited by blue or ultraviolet (UV) light, have been developed [7]. Some Eu-activated red phosphors, such as $CaAlSiN_3:Eu^{2+}$ and $M_2Si_5N_8:Eu^{2+}$ (M = Ca, Sr, or Ba), have also been synthesized for practical use [8,9]. These phosphors not only have strong absorption and emission in the visible-light range but also high chemical stability. Their photoluminescence (PL) intensity at 150 °C is over 80%, indicating that they are suitable for use in high-color-rendering white LEDs. The PL properties and full width at half-maximum of nitride phosphors are modulated in the visible-light range by the crystal field [10,11]. The crystal field around the luminescence center depends on the host material. Therefore, the search of new nitride host materials is a burgeoning research field [12].

Eu^{3+}-doped phosphors have absorption bands in the UV and blue-light region and exhibit red luminescence [13,14]. However, their luminescence efficiency is low because the absorption and emission are derived from a forbidden transition [15]. The quantum efficiency of Y_2O_3 in practical applications is relatively low at ~10% under UV (394 nm) or blue-light (466 nm) irradiation [16] compared to that of $Y_3Al_5O_{12}:Ce^{3+}$ phosphor [17]. Increasing the activator content in phosphors could address the low luminescence efficiency. However, a high activator content leads to the concentration quenching effect, resulting in low luminescence efficiency [18]. In Eu^{3+}, the exchange

interaction between Eu^{3+} ions is effective when the distance between activators is <5 Å [19]. Therefore, it is preferable to select a crystal structure that can maintain the distance between the Eu^{3+} activators at >5 Å.

A few garnet-type phosphors with heavy Eu doping, such as $Ca_2YSc_2GaSi_2O_{12}:Eu^{3+}$ [20], $Li_3Y_3Te_2O_{12}:Eu^{3+}$ [21], $Li_6CaLa_2Sb_2O_{12}:Eu^{3+}$ [22], and $Ca_2LaHf_2Al_3O_{12}:Eu^{3+}$ [23], have been used in high-color-rendering white LEDs. Eu constitutes the host material of the garnet and occupies the eight-coordinated dodecahedral sites in the garnet-type structure. As shown in Fig. 2.1, each dodecahedron shares edges with four dodecahedra (e.g., the No. 3 dodecahedron shares edges with the No. 1, 2, 4, and 5 dodecahedra). To prevent electrostatic repulsion between the cations sharing edges, Eu^{3+} tends to occupy only every other dodecahedral sites (e.g., the No. 2 and 5 sites or the No. 1 and 4 sites). These distances, which are approximately 7 Å [24], may suppress concentration quenching.

Controlling the emission wavelengths of LEDs is useful for further applications. Phosphors emitting red light near 600 nm have good visibility and are suitable for application in high-color-rendering white LEDs [25,26]. The infrared wavelength near 700 nm is suitable for plant growth [27]. The emission intensities of the $^5D_0 \rightarrow {}^7F_2$ (~610 nm) and $^5D_0 \rightarrow {}^7F_4$ (~710 nm) transitions in Eu^{3+} depend on the coordination environment [28]. When Eu^{3+} occupies the site close to the D_{4d} symmetry, the intensity of the $^5D_0 \rightarrow {}^7F_4$ transition is high [28,29]. A rotation of the top square face of the cube relative to its base plane from 0° to 45° results in a square antiprism with D_{4d} symmetry, as shown in Fig. 2.2 [30].

Judd and Ofelt theoretically elucidated the electric dipole transition of rare earth ions [31,32]. The spontaneous emission probability is described by three parameters, Ω_λ,

where λ = 2, 4, and 6. In garnet-type structures, a rotation of the top and bottom faces of the eight-coordinated dodecahedron leads to a decrease in the Ω_2/Ω_4 ratio, resulting in an intense $^5D_0 \rightarrow {}^7F_4$ transition [33]. However, there have been no experimental reports that elucidate the relationship between the distortion of the dodecahedron around Eu in garnet-type structures and the Ω_2/Ω_4 ratio. To explain changes in emission due to the coordination environment around Eu, it is necessary to describe the changes in the rotation angles of the top and bottom faces of the dodecahedron when the sizes of the cations surrounding the site vary.

In this study, $Ca_2EuZr_{2-x}Sn_xGa_3O_{12}$ (x = 0, 0.5, 1, 1.5, and 2) phosphors were synthesized through a solid-state reaction. Zr and Sn can modify the environment around Eu^{3+} because of differences in electronegativity (Zr: 1.22 and Sn: 1.72 [34]) and ionic radius (Zr^{4+}: 0.72 Å and Sn^{4+}: 0.69 Å [35]). We propose a method to describe the rotation angles of the top and bottom faces of the eight-coordinated dodecahedron in a garnet-type structure based on simple geometric calculations utilizing the ratios of the edges of the dodecahedron. We investigate the change in emission wavelength of Eu^{3+} due to a variation in the Sn and Zr content in garnet-type $Ca_2EuZr_{2-x}Sn_xGa_3O_{12}$ phosphors.

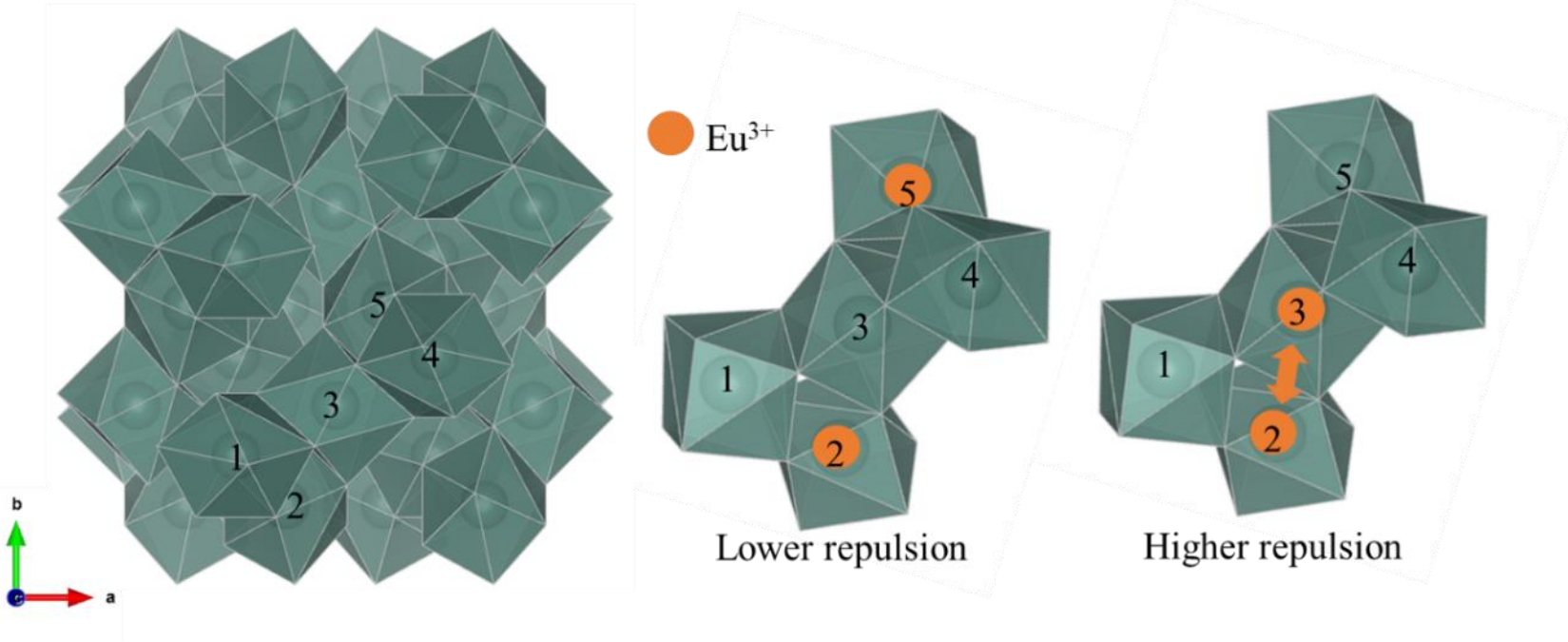

Fig. 2.1 Framework of the eight-coordinated dodecahedra in the garnet-type structure. Eu^{3+} may occupy these sites with one skip to prevent electrostatic repulsion.

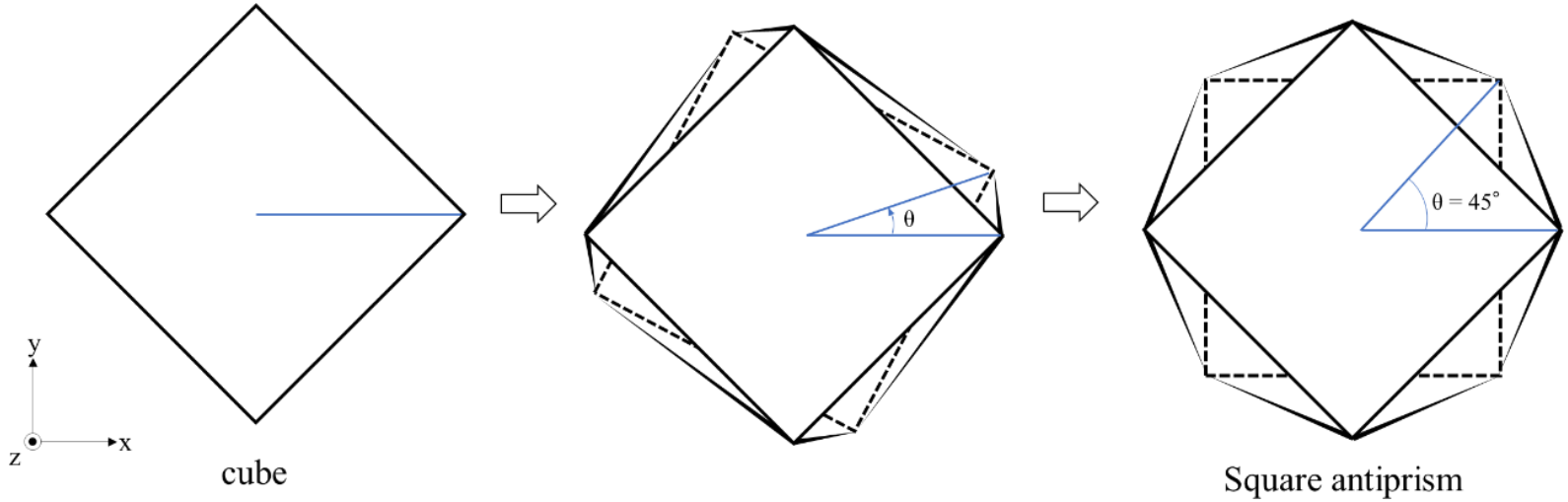

Fig. 2.2 Change from a cube to a square antiprism (top view of the polyhedron). Rotation of the top square face of the cube relative to its base plane from 0° to 45°, resulting in a square antiprism with D_{4d} symmetry.

2.2 Sample synthesis

$Ca_2EuZr_{2-x}Sn_xGa_3O_{12}$ (x = 0, 0.5, 1, 1.5, and 2) phosphors were synthesized via a solid-state reaction. Stoichiometric quantities of $CaCO_3$ (99.99%, Kojundo Chemical, Japan), Eu_2O_3 (99.95%, Kanto Chemical, Japan), ZrO_2 (99.0%, Kanto Chemical, Japan), SnO_2 (98.0%, Kanto Chemical, Japan), and Ga_2O_3 (99.995%, Yamanaka Hutech Corporation, Japan) were ground and mixed in an agate mortar for 40 min. After calcination at 1200 °C for 4 h, the mixture was cooled to room temperature (RT). Finally, the mixture was calcined at 1500 °C for 4 h to obtain the desired products.

2.3 Characterization

The crystalline structures of the phosphors were investigated at RT via powder X-ray diffraction (XRD, SmartLab X-ray Diffractometer, Rigaku, Japan) with Cu-Kα radiation at 45 kV and 200 mA in the 2θ range of 10°–90°. Rietveld analysis was conducted using RIETAN-FP software [36]; a step scanning technique was adopted within the 2θ range of 10°–120° with an increment of 0.01°. The particle shape and size were determined using scanning electron microscopy (SEM, JSM-6390, JEOL, Japan). The particle size distribution was calculated by counting and measuring 300 particles using the ImageJ software. The luminescence properties of all the phosphors were measured using fluorescence spectrometry (FP-8300 Spectrofluorometer, JASCO, Japan), wherein the excitation and monitored wavelengths were 395 and 610 nm, respectively.

2.4 Results and Discussion

XRD patterns and Rietveld analysis

The XRD patterns of the $Ca_2EuZr_{2-x}Sn_xGa_3O_{12}$ (x = 0, 0.5, 1, 1.5, and 2) phosphors calcined at 1500 °C for 4 h are shown in Fig. 2.3. The XRD patterns of the samples are consistent with the Joint Committee on Powder Diffraction Standards (JCPDS) card of $Ca_3Zr_2(Fe_{1.5}Al_{0.5}Si)O_{12}$ [37], confirming the formation of the garnet-type structure. Fig. 2.3(b) shows the XRD patterns of the samples at high angles. In samples with x = 0 and 2, the diffraction peaks shifted to higher angles due to lattice shrinking originating from the difference in the ionic radii. By contrast, the diffraction peaks of the samples with x = 0.5, 1, and 1.5 were broad, indicating that the formation of solid solution was difficult.

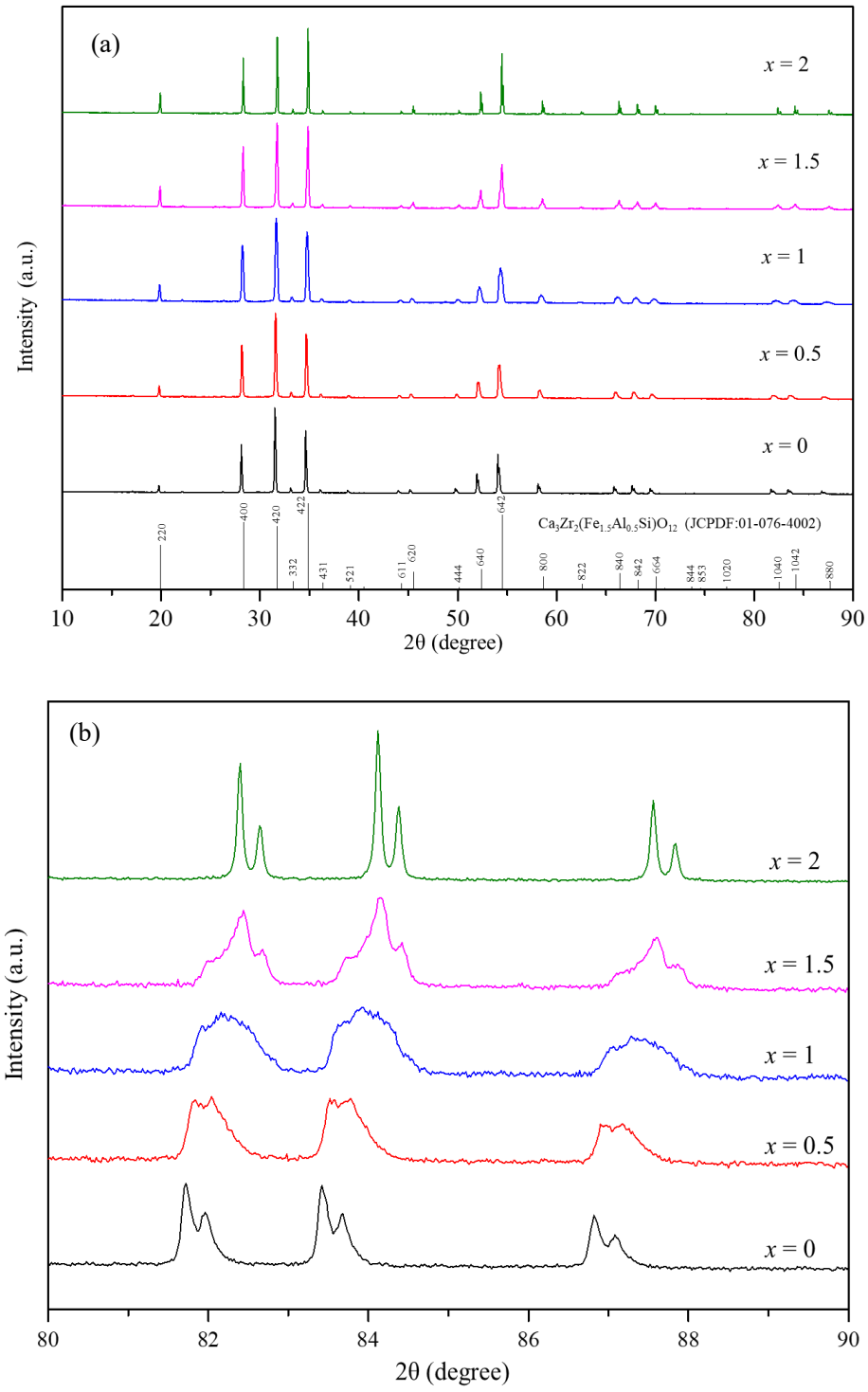

Fig. 2.3 XRD patterns of $Ca_2EuZr_{2-x}Sn_xGa_3O_{12}$ (x = 0, 0.5, 1, 1.5, and 2) with 2θ in the range of (a) 10°–90° and (b) 80°–90°.

Rietveld analysis was conducted for the samples with $x = 0$ and 2 using RIETAN-FP software. The crystal system of the garnet-type structure was assumed to be cubic with a space group of *Ia*-3*d* (No. 230). The garnet-type structure ($A_3B_2C_3O_{12}$) consists of three polyhedra: eight-coordinated dodecahedral (Wyckoff position: 24c, fractional coordinate (1/8, 0, 1/4)); six-coordinated octahedral (Wyckoff position: 16a, fractional coordinate (0, 0, 0)); and four-coordinated tetrahedral sites (Wyckoff position: 24d, fractional coordinate (3/8, 0, 1/4)). The Wyckoff position and fractional coordinate of oxygen are 96h and (x, y, z), respectively. The lattice constant, thermal parameters of each site, and fractional coordinate of oxygen were refined after optimizing the scale, background, profile, and half-width.

The Rietveld refinement of the garnet-type $Ca_2EuZr_2Ga_3O_{12}$ was conducted assuming that 2/3 Ca and 1/3 Eu occupied the dodecahedral site, Zr occupied the octahedral site, and Ga occupied the tetrahedral site. The thermal parameters of Ca and Eu at the dodecahedral site were constrained to possess the same value. The results of Rietveld refinement of the garnet-type $Ca_2EuZr_2Ga_3O_{12}$ are summarized in Table 2.1 and Fig. 2.4. The calculation results were in good agreement with the experimental XRD pattern.

The Rietveld refinement of garnet-type $Ca_2EuSn_2Ga_3O_{12}$ was conducted under the assumptions that 2/3 Ca and 1/3 Eu occupied the dodecahedral site, Sn occupied the octahedral site, and Ga occupied the tetrahedral site. The thermal parameters of Ca and Eu at the dodecahedral site were constrained to have the same value. However, the refinement diverged during the analysis. The calculation results (shown in Table 2.2 and Fig. 2.5) did not agree with the experimental XRD pattern, and the thermal parameters were negative. The similarity between the ionic radius and electronegativity of Sn^{4+} and

Ga^{3+} is higher than that between Zr^{4+} and Ga^{3+}. Therefore, cation mixing of Sn^{4+} and Ga^{3+} may have occurred in garnet-type $Ca_2EuSn_2Ga_3O_{12}$.

The refinement of garnet-type $Ca_2EuSn_2Ga_3O_{12}$ was conducted again with the assumptions that 2/3 Ca and 1/3 Eu occupied the dodecahedral site and both Sn and Ga occupied the octahedral and tetrahedral sites. The thermal parameters of Ca and Eu occupying the dodecahedral site were constrained to be equal, those of Ga and Sn occupying the octahedral site were constrained to be equal, and those of Ga and Sn occupying the tetrahedral site were constrained to be equal.

The refinement reached completion and indicated the structure $Ca_2Eu[Sn_{1.9}Ga_{0.1}]_{oct}(Ga_{2.9}Sn_{0.1})_{tet}O_{12}$, as shown in Table 2.3 and Fig. 2.6. This implies that Sn and Ga occupied both the octahedral and tetrahedral sites in the garnet-type structure. The occupancy of Sn at each site was evaluated by trial and error. We refined four models of the garnet-type structure: $Ca_2Eu[Sn_{1.95}Ga_{0.05}]_{oct}(Ga_{2.95}Sn_{0.05})_{tet}O_{12}$ (CESG0.05), $Ca_2Eu[Sn_{1.9}Ga_{0.1}]_{oct}(Ga_{2.9}Sn_{0.1})_{tet}O_{12}$ (CESG0.1), $Ca_2Eu[Sn_{1.8}Ga_{0.2}]_{oct}(Ga_{2.8}Sn_{0.2})_{tet}O_{12}$ (CESG0.2), and $Ca_2Eu[Sn_{1.7}Ga_{0.3}]_{oct}(Ga_{2.7}Sn_{0.3})_{tet}O_{12}$ (CESG0.3). The refinement of CESG0.05 diverged during the analysis, suggesting that its initial occupancy values were incorrect. Moreover, the value of the thermal parameter at the dodecahedral site was significantly higher than that at other sites in the models CESG0.2 and CESG0.3. Therefore, we concluded that the CESG0.1 model was the best. However, the relative intensities of the three main peaks still differed in the measured and calculated profiles. To achieve further refinement of the atomic positions and occupancies, collecting X-ray diffraction data using synchrotron radiation and chemical composition analysis will be necessary.

For the x = 0, 1.0, and 1.5 samples, the 420 peak has the highest intensity,

whereas the 422 peak has the highest intensity for the $x = 2$ sample. This variation in the diffraction peak intensity can be ascribed to differences in the structure factors. It is evident from Fig. 2.7 that the (420) plane has cations occupying only the octahedral sites, while the (422) crystallographic plane contains cations occupying both the octahedral and tetrahedral sites. From the Rietveld analysis results, Zr occupied only the octahedral sites in the $Ca_2EuZr_2Ga_3O_{12}$ phosphor, whereas Sn occupied both the octahedral and tetrahedral sites in the $Ca_2EuSn_2Ga_3O_{12}$ phosphor. The relatively higher atomic scattering factor of Sn [38], which occupies both the octahedral and tetrahedral sites, likely enhances the intensity of the 422 peak relative to that of the 420 peak.

The Rietveld analysis revealed that the distribution of cations at the octahedral and tetrahedral sites in the garnet-type structure is different in the $x = 0$ and 2 samples. Zr occupies only the octahedral sites and Ga occupies only the tetrahedral sites in the $x = 0$ sample, whereas in the $x = 2$ sample, Sn and Ga occupy both octahedral and tetrahedral sites. The broad peaks in the XRD patterns of the $x = 0.5$, 1, and 1.5 samples might be due to the differences in compositional uniformity at the octahedral and tetrahedral sites in the garnet-type structure, which prevent the formation of a solid solution.

Table 2.1 Details of data collection, refinement, and fractional atomic coordinates of $Ca_2EuZr_2Ga_3O_{12}$ at RT.

Atom	Site	Site occupancy	x	y	z	B(Å²)
Ca	24c	2/3	1/8	0	1/4	2.162(46)
Eu	24c	1/3	1/8	0	1/4	
Zr	16a	1	0	0	0	2.004(23)
Ga	24d	1	3/8	0	1/4	1.860(46)
O	96h	1	0.34631(16)	0.46859(20)	0.05366(16)	1.594(72)

Formula	$Ca_2EuZr_2Ga_3O_{12}$
Structure type	Garnet-type structure
Space group(Number)	Ia-3d(#230)
Date range(/ ° 2θ)	10-120
Step size(/ ° 2θ)	0.01
Number of date points	11001
a/Å	12.68607(7)
Z	8
R_{wp}	4.763
R_e	5.178
S	0.9199

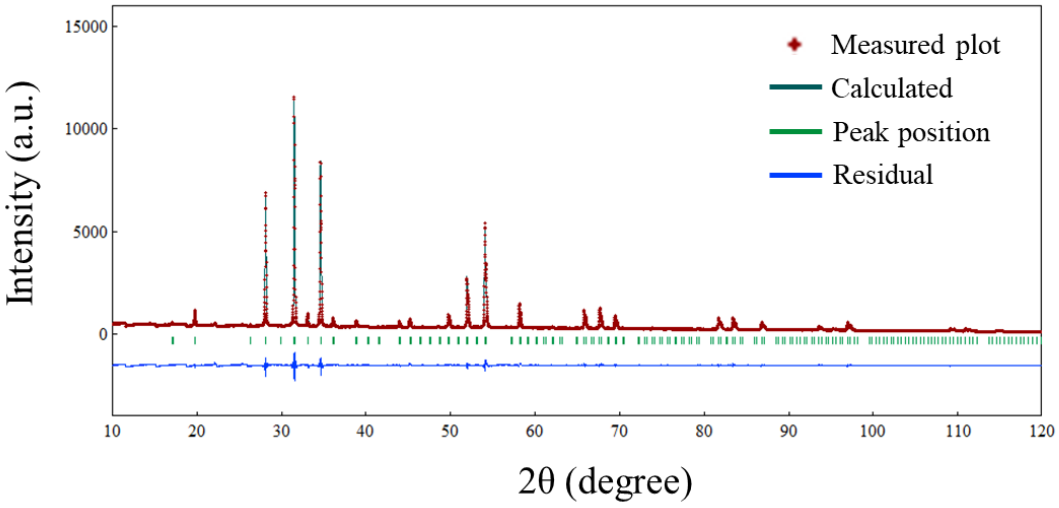

Fig. 2.4 Rietveld refinement of $Ca_2EuZr_2Ga_3O_{12}$.

Table 2.2 Details of data collection, refinement, and fractional atomic coordinates of $Ca_2EuSn_2Ga_3O_{12}$ at room temperature.

Atom	Site	Site occupancy	x	y	z	B(Å²)
Ca	24c	2/3	1/8	0	1/4	-2.98322
Eu	24c	1/3	1/8	0	1/4	
Sn	16a	1	0	0	0	-0.365
Ga	24d	1	3/8	0	1/4	1.0
O	96h	1	0.34	0.45	0.05	1.0

Formula	$Ca_2EuSn_2Ga_3O_{12}$
Structure type	Garnet-type structure
Space group(Number)	Ia-3d(#230)
Date range(/ ° 2θ)	10-120
Step size(/ ° 2θ)	0.01
Number of date points	11001
a/Å	12.5996
Z	8
R_{wp}	65.155
R_e	5.800
S	11.2335

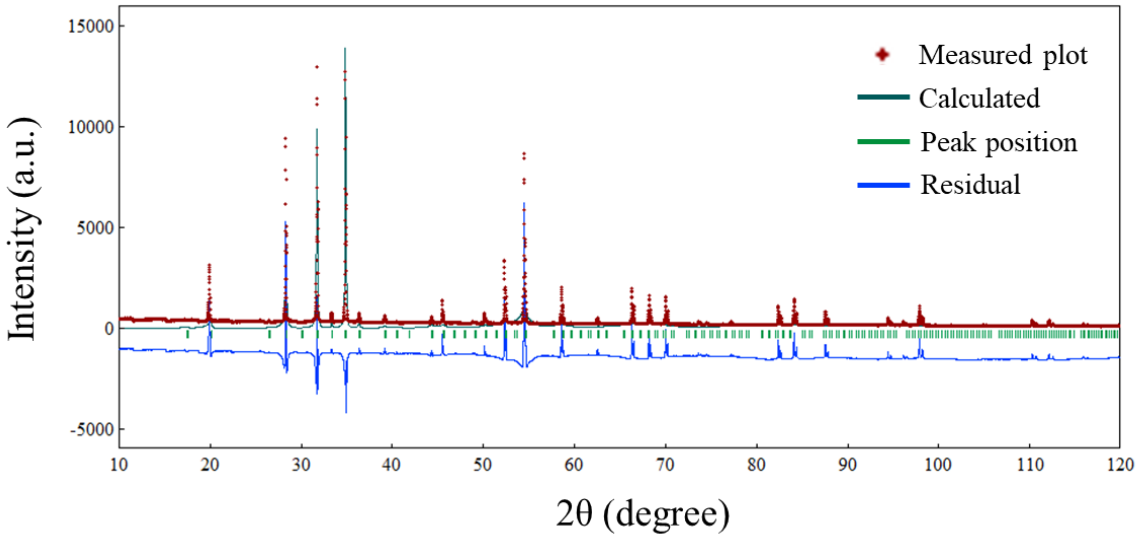

Fig. 2.5 Rietveld refinement plot of $Ca_2EuSn_2Ga_3O_{12}$.

Table 2.3 Details of data collection, refinement, and fractional atomic coordinates of $(Ca_2Eu)(Sn_{1.9}Ga_{0.1})(Ga_{2.9}Sn_{0.1})O_{12}$ at RT.

Atom	Site	Site occupancy	x	y	z	B(Å²)
Ca	24c	2/3	1/8	0	1/4	1.843(44)
Eu	24c	1/3	1/8	0	1/4	
Sn1	16a	19/20	0	0	0	1.868(17)
Ga1	16a	1/20	0	0	0	
Sn2	24d	1/30	3/8	0	1/4	2.366(50)
Ga2	24d	29/30	3/8	0	1/4	
O	96h	1	0.34798(16)	0.47057(24)	0.05247(19)	1.597(77)

Formula	$(Ca_2Eu)(Sn_{1.9}Ga_{0.1})(Ga_{2.9}Sn_{0.1})O_{12}$
Structure type	Garnet-type structure
Space group(Number)	Ia-3d(#230)
Date range(/ ° 2θ)	10-120
Step size(/ ° 2θ)	0.01
Number of date points	11001
a/Å	12.59719(5)
Z	8
R_{wp}	5.887
R_e	5.793
S	1.0161

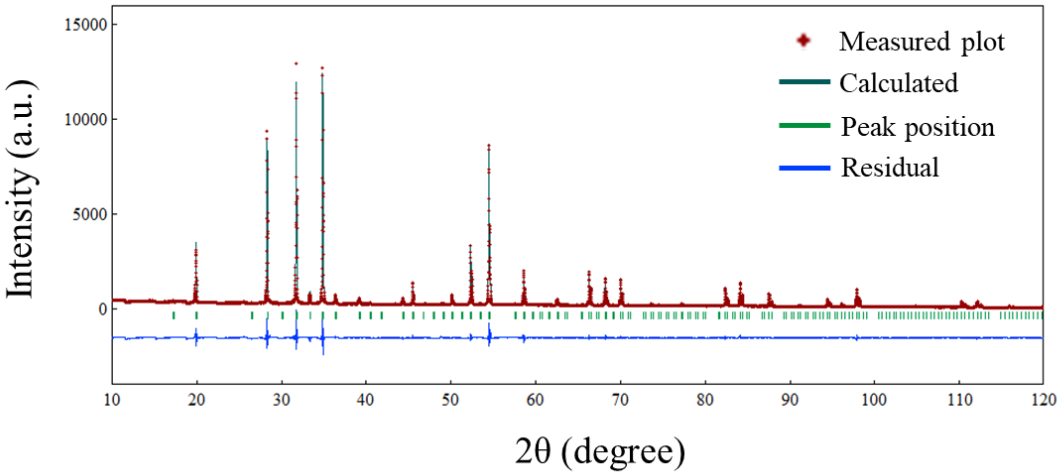

Fig. 2.6 Rietveld refinement of $(Ca_2Eu)(Sn_{1.9}Ga_{0.1})(Ga_{2.9}Sn_{0.1})O_{12}$.

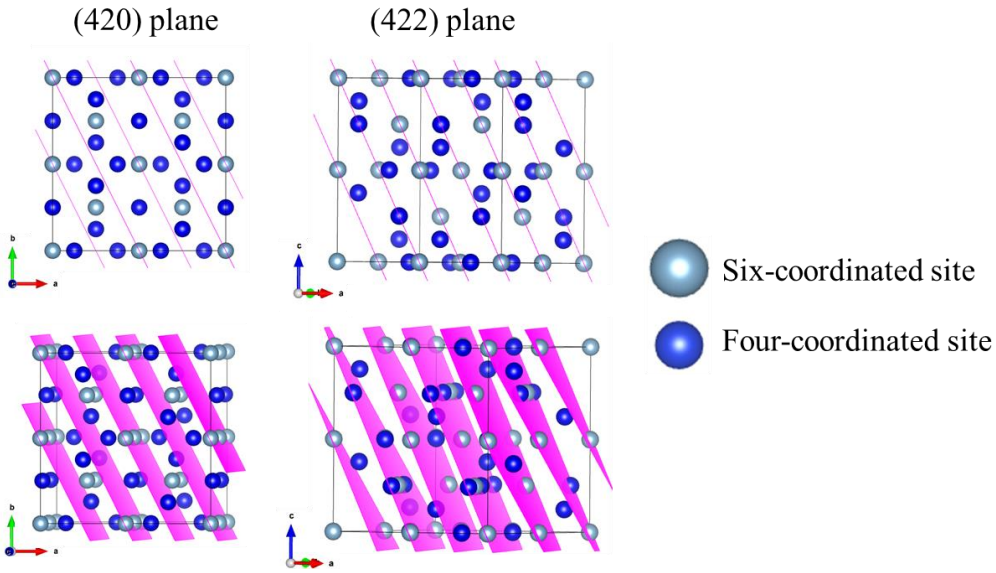

Fig. 2.7 (420) and (422) planes of the garnet-type structure. The (420) plane only has cations occupying six-coordinated sites, while the (422) crystallographic plane contains cations occupying both six- and four-coordinated sites.

SEM image

The SEM images and particle distributions of the $Ca_2EuZr_{2-x}Sn_xGa_3O_{12}$ (x = 0 and 2) phosphors are shown in Fig. 2.8. The particle size of the Zr-containing garnet was larger (9.31 ± 4.06 μm) than those of the Sn-containing garnet (2.78 ± 0.98 μm). Rietveld analysis revealed that cation mixing between Ga and Sn occurs at the octahedral and tetrahedral sites of the garnet-type structure in the $Ca_2EuSn_2Ga_3O_{12}$ phosphor, which might affect the particle growth. Correlations between cation mixing (or antisite defects) in the crystal structure and particle size distribution have been reported in cathode materials for lithium-ion batteries and magnetic materials [39–42].

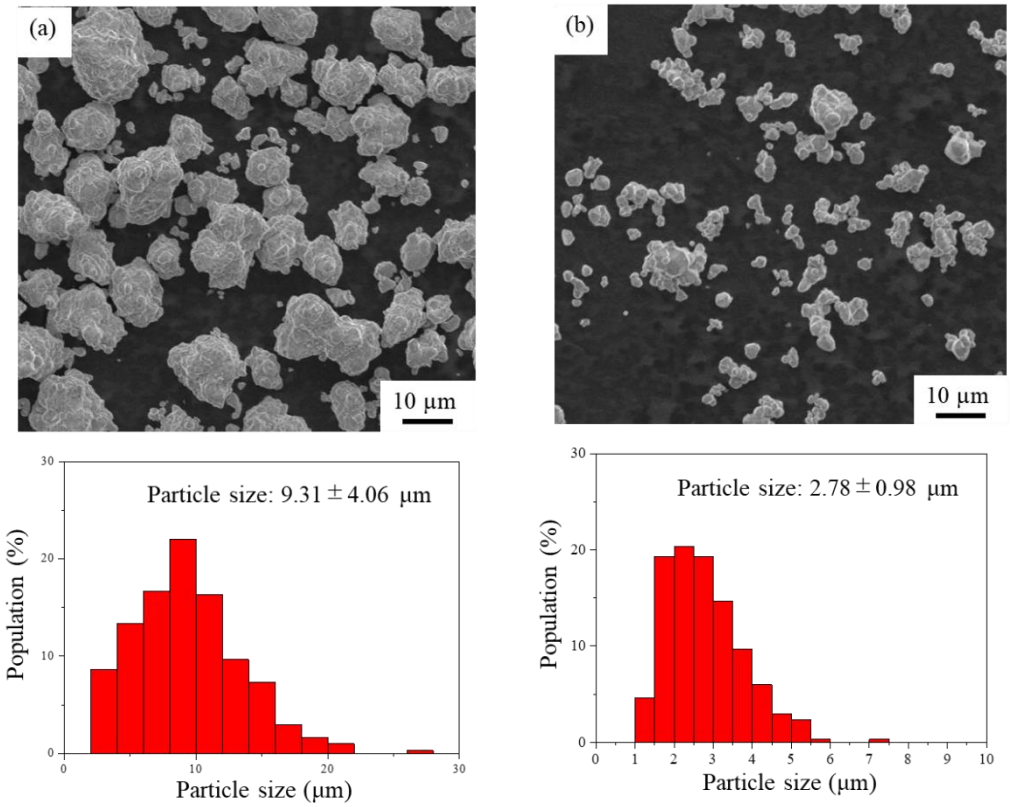

Fig. 2.8 SEM images and particle size distributions of (a) $Ca_2EuZr_2Ga_3O_{12}$ and (b) $Ca_2EuSn_2Ga_3O_{12}$.

PL measurement

Excitation and emission spectra of the $Ca_2EuZr_{2-x}Sn_xGa_3O_{12}$ (x = 0, 0.5, 1, 1.5, and 2) phosphors are shown in Fig. 2.9. The excitation bands monitored at 610 nm were observed from 200 to 500 nm in all samples. The broad excitation peak at approximately 280 nm is derived from a charge transfer band. The shape of the excitation peaks in the range from 300 to 500 nm are attributed to the f-f transition of Eu^{3+}. The excitation peak was located at ~395 nm, while the fluorescence spectra showed red emission at ~590, ~610, ~650, and ~710 nm under 395 nm UV irradiation; these emission bands are due to the f-f transitions $^5D_0 \rightarrow {}^7F_1$, $^5D_0 \rightarrow {}^7F_2$, $^5D_0 \rightarrow {}^7F_3$, and $^5D_0 \rightarrow {}^7F_4$, respectively [28]. The internal quantum efficiency of all samples was greater than 45%, which indicates that these phosphors have potential applications in high-color-rendering white LEDs via near-UV excitation.

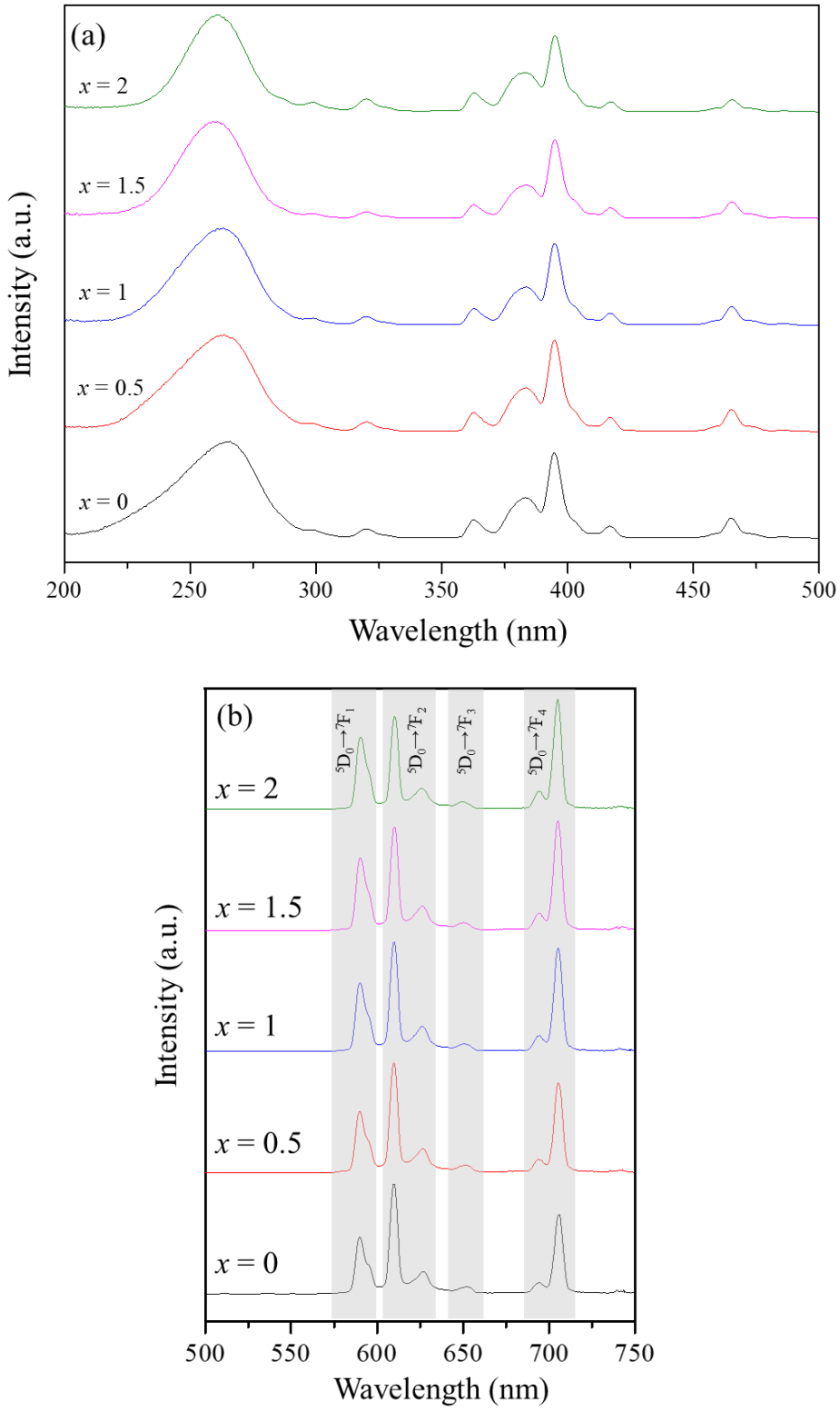

Fig. 2.9 (a) Excitation and (b) emission spectra of $Ca_2EuZr_{2-x}Sn_xGa_3O_{12}$ (x = 0, 0.5, 1, 1.5, and 2).

Emission modulation of Eu^{3+} via symmetry around dodecahedron in garnet-type structure

The radiative transition probabilities A_R of the $^5D_0 \rightarrow {}^7F_J$ (J = 2 and 4) transitions and the corresponding emission peak area S are related by the following equation [43]:

$$\frac{A_R(5D_0 \rightarrow 7F_2)}{A_R(5D_0 \rightarrow 7F_4)} = \frac{S(5D_0 \rightarrow 7F_2)}{S(5D_0 \rightarrow 7F_4)} \quad (1)$$

The radiative transition probabilities A_R of the $^5D_0 \rightarrow {}^7F_J$ (J = 2 and 4) transitions can also be written as [43]:

$$A_R(5D_0 \rightarrow 7F_2) = \frac{64\pi^4 e^2 \upsilon_2^3}{3h(2J+1)}\left[\frac{n(n^2+2)^2}{9}\right]\Omega_2\left\|U^{(2)}\right\|^2 \quad (2)$$

$$A_R(5D_0 \rightarrow 7F_4) = \frac{64\pi^4 e^2 \upsilon_4^3}{3h(2J+1)}\left[\frac{n(n^2+2)^2}{9}\right]\Omega_4\left\|U^{(4)}\right\|^2 \quad (3)$$

where e is the charge of an electron, n is the refractive index, v is the emission peak wavenumber, h is the Planck constant, and J is the total angular momentum quantum number of the initial energy level $^5D_0$. $\left\|U^{(J)}\right\|^2$ denote the reduced matrix elements from the initial to the excited state, which have an intrinsic value ($\left\|U^{(2)}\right\|^2$= 0.0032 and $\left\|U^{(4)}\right\|^2$= 0.0023 [44]). The ratio of the intensity parameters Ω_2 and Ω_4 is given by the equation:

$$\frac{\Omega_2}{\Omega_4} = \frac{S(5D_0 \rightarrow 7F2)}{S(5D_0 \rightarrow 7F4)} \times \frac{\left\|U^{(4)}\right\|^2}{\|U^{(2)}\|^2} \times \left(\frac{\upsilon_4}{\upsilon_2}\right)^3 \quad (4)$$

Fig. 2.10 shows the correlation between Ω_2/Ω_4 and x for $Ca_2EuZr_{2-x}Sn_xGa_3O_{12}$ (x = 0,

0.5, 1, 1.5, and 2). The Ω_2/Ω_4 ratio decreased with an increase in the value of x.

The coordination environment around Eu^{3+} has a significant influence on the intensity of the $^5D_0 \rightarrow {}^7F_4$ transition [28,29]. The intensity of the $^5D_0 \rightarrow {}^7F_4$ transition is high when Eu^{3+} occupies the crystallographic site with D_{4d} point symmetry. Li et al. [45] reported that the intense $^5D_0 \rightarrow {}^7F_4$ transition observed in Eu^{3+}-doped $Ca_2Ga_2GeO_7$ phosphor is due to Eu^{3+} occupying the dodecahedral site wherein the geometry was distorted from cubic to square antiprism. Bettinelli et al. [33] reported that rotation of the top and bottom faces of the dodecahedron in the garnet-type structure leads to a decrease in the ratio of the intensity parameter of the Judd–Ofelt theory (Ω_2/Ω_4), resulting in a high-intensity $^5D_0 \rightarrow {}^7F_4$ transition.

As the bottom of the cube is rotated from 0° to 45° relative to its top, the geometry approaches a square antiprism with D_{4d} symmetry. The lengths of the edges connecting the vertices of the top and bottom surfaces in the cube and square antiprism also change continuously with the rotation of the surfaces. As shown in Fig. 2.11, the d_L/d_S ratio is related to the rotation angle of the bottom surface relative to the top surface by the following equation:

$$d_L/d_S = \sqrt{\frac{2 - \sin\theta}{2 - \cos\theta}} \tag{5}$$

The derivation of the equation is as follows:

Consider a cube with side length $\sqrt{2}R$, a distance h between the top and bottom surfaces, Eu^{3+} at the center, and oxide ions coordinated at the vertices; the fractional coordinates of oxide ions O1, O2, and O3 are expressed as in Fig. 2.11 when the position of Eu^{3+} is the origin, and the rotation angle between the top and bottom surfaces is θ. The lengths of d_L and d_S are expressed using the vectors $\vec{a}$, $\vec{b}$, and $\vec{c}$ as follows ($\vec{a}$, $\vec{b}$, and $\vec{c}$ are defined

as the vector from the origin to O1, O2, and O3, respectively):

$$d_{\mathrm{L}} = \left|\vec{b} - \vec{c}\right| = \sqrt{2R^2(1 - \sin\theta) + h^2} \quad (1)$$

$$d_{\mathrm{S}} = \left|\vec{a} - \vec{b}\right| = \sqrt{2R^2(1 - \cos\theta) + h^2} \quad (2)$$

The ratio of d_{L} and d_{S} is represented as

$$\boldsymbol{d_L/d_S} = \sqrt{\frac{2R^2(1 - \sin\theta) + h^2}{2R^2(1 - \cos\theta) + h^2}} \quad (\mathbf{3})$$

When the distance h between the top and bottom faces is equal to side length $\sqrt{2}R$ of the cube, $d_{\mathrm{L}}/d_{\mathrm{S}}$ is expressed as follows:

$$\boldsymbol{d_L/d_S} = \sqrt{\frac{2R^2(1 - \sin\theta) + 2R^2}{2R^2(1 - \cos\theta) + 2R^2}} = \sqrt{\frac{2 - sin\theta}{2 - cos\theta}} \quad (\mathbf{4})$$

Here, d_{S} is defined as the distance between O1 and O2 in Fig. 2.11, while d_{L} is defined as the distance between O2 and O3 in the same figure. The $d_{\mathrm{L}}/d_{\mathrm{S}}$ ratio ranges from $\sqrt{2}$ to 1 as the rotation angle changes from 0° to 45°, corresponding to a cube and a square antiprism, respectively. Fig. 2.12 shows correlation between the rotation angle θ and $d_{\mathrm{L}}/d_{\mathrm{S}}$. This equation is valid for the dodecahedron in garnet-type structures, where the faces enclosed by the shared edges of the two dodecahedra and the two octahedra are the top and bottom surfaces, respectively, and the shared edges of the tetrahedra correspond to length d_{S} (Fig. 2.13).

Rietveld analysis revealed that Zr occupied only the octahedral site in the $Ca_2EuZr_2Ga_3O_{12}$ phosphor, whereas Sn occupied both the tetrahedral and octahedral sites in the $Ca_2EuSn_2Ga_3O_{12}$ phosphor. The ionic radius of Sn^{4+} (0.69 Å) is larger than that of Ga^{3+} (0.47 Å) [35]. Hence, Sn^{4+} at the tetrahedral site increases the d_{S} length, resulting in a smaller $d_{\mathrm{L}}/d_{\mathrm{S}}$ ratio. The $d_{\mathrm{L}}/d_{\mathrm{S}}$ ratios for the $Ca_2EuZr_2Ga_3O_{12}$ and $Ca_2EuSn_2Ga_3O_{12}$

phosphors are 1.31 and 1.30, respectively and correspond to rotation angles of 14° and 15°. These results indicate that the symmetry around Eu^{3+} at the dodecahedral site approached a square antiprism geometry, resulting in a decreasing Ω_2/Ω_4 ratio with increasing Sn content in the garnet-type $Ca_2EuZr_{2-x}Sn_xGa_3O_{12}$ phosphors. The decrease in the Ω_2/Ω_4 ratio with increasing x is attributed to the increase in the ratio of the Sn-containing garnet phase that emits at ~710 nm, which is due to the $^5D_0 \rightarrow {}^7F_4$ transition. This relationship between the rotation angle and the d_L/d_S ratio may be applied in the analysis of other garnet-type structures. Skaudzius et al. [46] investigated the intensity of the $^5D_0 \rightarrow {}^7F_4$ transition in garnets it is lower in Eu^{3+}-doped $Y_3Al_5O_{12}$ than that in Eu^{3+}-doped $Y_3Ga_5O_{12}$. The d_L/d_S ratios of $Y_3Al_5O_{12}$ and $Y_3Ga_5O_{12}$ were calculated from the values reported by Nakatsuka et al. [47,48]. The d_L/d_S ratios of $Y_3Al_5O_{12}$ and $Y_3Ga_5O_{12}$ are 1.29 and 1.27, respectively, and correspond to rotation angles of 16° and 18°. Therefore, the d_L/d_S ratios in the garnet-type structure are related to the symmetry of the dodecahedron and can help estimate the intensity of the $^5D_0 \rightarrow {}^7F_4$ transition.

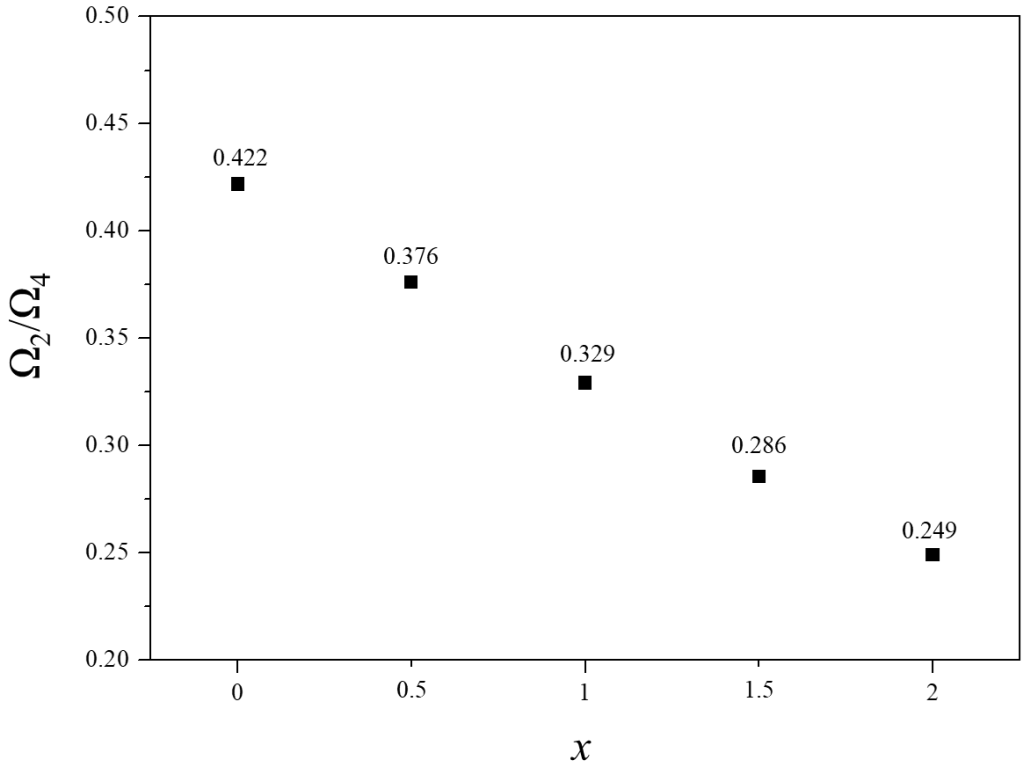

Fig. 2.10 Correlation between x and Ω_2/Ω_4.

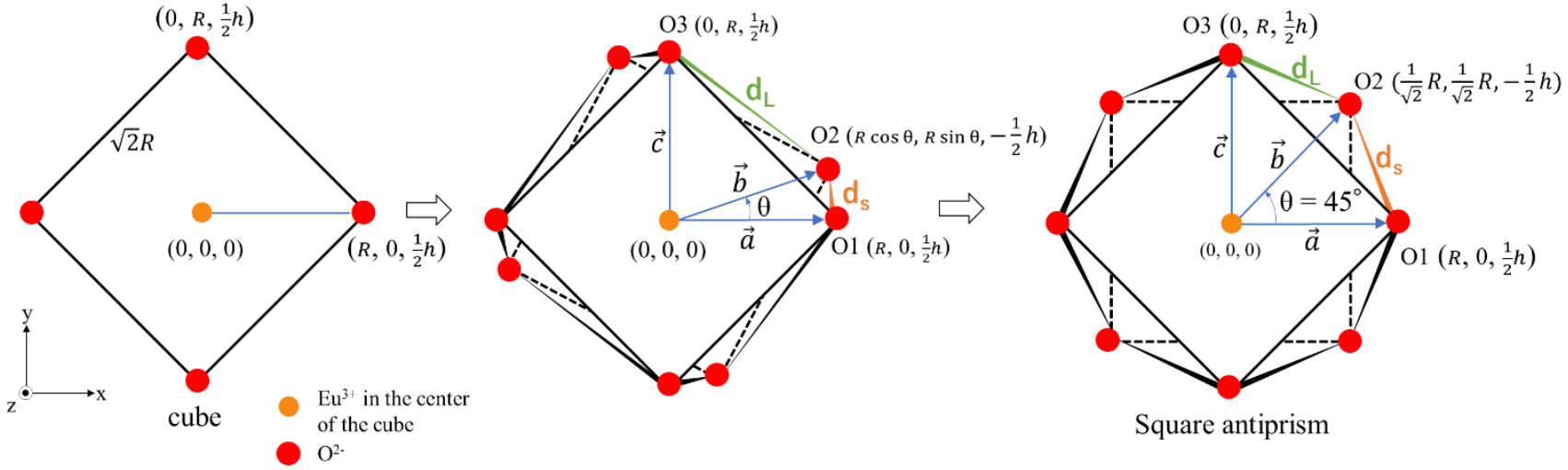

Fig. 2.11 The change from a cube to a square antiprism when $\theta = 0°$, $0° \leq \theta \leq 45°$, and $\theta = 45°$.

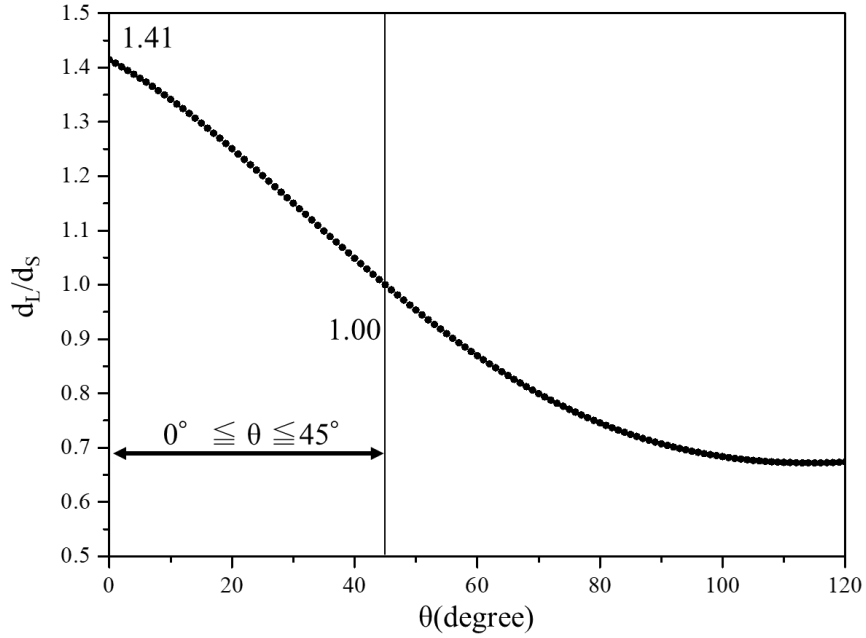

Fig. 2.12 Correlation between the rotation angle θ and d_L/d_S. In the range $0° \leq \theta \leq 45°$, d_L/d_S gradually decreases with increasing rotation angle.

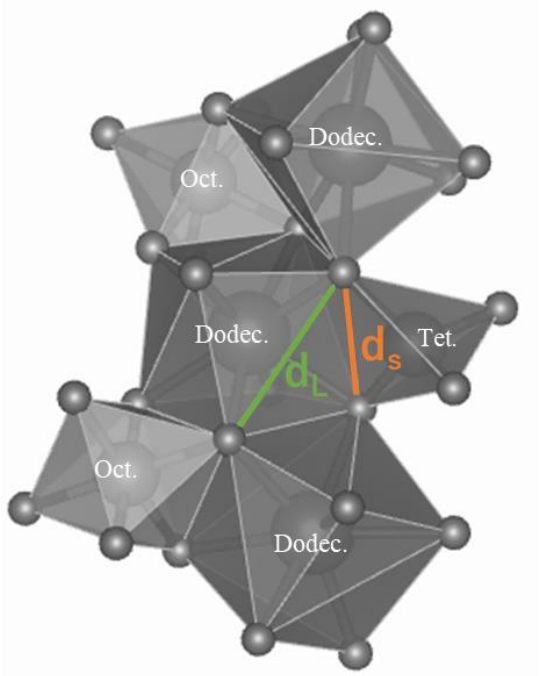

Fig. 2.13 Illustration of d_L and d_S in the garnet-type structure. In the case of Sn-containing garnet, Sn^{4+} increased d_S (because the ionic radius of Sn^{4+} is larger than that of Ga^{3+}), resulting in the coordination environment around Eu^{3+} approaching a square antiprism geometry.

References

[1] E.F. Schubert, J.K. Kim, *Science* **308** (2005) 1274–1278.

[2] C.J. Humphreys, *MRS Bull.* **33** (2008) 459–470.

[3] C.C. Lin, R.S. Liu, *J. Phys. Chem. Lett.* **2** (2011) 1268–1277.

[4] S. Nakamura, T. Mukai, M. Senoh, *Appl. Phys. Lett.* **64** (1994) 1687–1689.

[5] Z. Xia, A. Meijerink, *Chem. Soc. Rev.* **46** (2017) 275–299.

[6] Z. Xia, Q. Liu, *Prog. Mater. Sci.* **84** (2016) 59–117.

[7] Y. Zhang, L. Luo, G. Chen, Y. Liu, R. Liu, X. Chen, *J. Rare Earths* **38** (2020) 1–12.

[8] K. Uheda, N. Hirosaki, H. Yamamoto, *Phys. Status Solidi A* **203** (2006) 2712–2717.

[9] Y.Q. Li, J.E.J. van Steen, J.W.H. van Krevel, G. Botty, A.C.A. Delsing, F.J. DiSalvo, G. de With, H.T. Hintzen, *J. Alloys Compd.* **417** (2006) 273–279.

[10] R.-J. Xie, N. Hirosaki, *Sci. Technol. Adv. Mater.* **8** (2007) 588–600.

[11] S. Li, R.-J. Xie, T. Takeda, N. Hirosaki, *ECS J. Solid State Sci. Technol.* **7** (2018) R3064–R3078.

[12] T. Takeda, R.-J. Xie, T. Suehiro, N. Hirosaki, *Prog. Solid State Chem.* **51** (2018) 41–51.

[13] H. Chen, J. Wang, Y. Gao, S. Ai, Z. Wu, T. Zhou, M. Liu, Y. Zhao, X. Lai, J. Bi, D. Gao, *J. Alloys Compd.* **887** (2021) 161343.

[14] K. Liu, H. Chen, M. Tsai, Y. Chang, *Microsyst. Technol.* **24** (2018) 4043–4048.

[15] O. Laporte, W.F. Meggers, *J. Opt. Soc. Am.* **11** (1925) 459–463.

[16] S. Long, J. Hou, G. Zhang, F. Huang, Y. Zeng, *Ceram. Int.* **39** (2013) 6013–6017.

[17] Q. Yao, X. Pan, J. Tian, Z. Chen, H. Ji, Y. Wang, *Materials* **16** (2023) 730.

[18] D.L. Dexter, J.H. Schulman, *J. Chem. Phys.* **22** (1954) 1063–1070.

[19] J. Hu, X. Gong, J. Huang, Y. Chen, Y. Lin, Z. Luo, Y. Huang, *Opt. Mater. Express* **6** (2016) 181–190.

[20] P. Loiko, N. Khaidukov, A. Volokitina, I. Zhidkova, E. Vilejshikova, A. Novichkov, V. Aseev, J.M. Serres, X. Mateos, K. Yumashev, *Dyes Pigm.* **150** (2018) 158–164.

[21] W. Zhang, H.J. Seo, *J. Alloys Compd.* **553** (2013) 183–187.

[22] J. Zhong, D. Chen, W. Zhao, Y. Zhou, H. Yu, L. Chen, Z. Ji, *J. Mater. Chem. C* **3** (2015) 4500–4510.

[23] N. Ma, W. Li, B. Devakumar, X. Huang, *Inorg. Chem.* **61** (2022) 6898–6909.

[24] S. Geller, *Z. Kristallogr.* **125** (1967) 1–47.

[25] A. Stockman, L.T. Sharpe, *Vision Res.* **40** (2000) 1711–1737.

[26] F. Zhang, K. Kurokawa, A. Lassoued, J.A. Crowell, D.T. Miller, *Proc. Natl Acad. Sci. U. S. A.* **116** (2019) 7951–7956.

[27] Z. Yan, X. Yang, S. Xiao, *Mater. Res. Bull.* **133** (2021) 111040.

[28] K. Binnemans, *Coord. Chem. Rev.* **295** (2015) 1–45.
[29] R.A.S. Sá Ferreira, S.S. Nobre, C.M. Granadeiro, H.I.S. Nogueira, L.D. Carlos, O.L. Malta, *J. Lumin.* **121** (2006) 561–567.
[30] V.S. Mironov, Y.G. Galyametdinov, A. Ceulemans, C. Görller-Walrand, K. Binnemans, *J. Chem. Phys.* **116** (2002) 4673–4685.
[31] B.R. Judd, *Phys. Rev.* **127** (1962) 750–761.
[32] G.S. Ofelt, *J. Chem. Phys.* **37** (1962) 511–520.
[33] M. Bettinelli, A. Speghini, F. Piccinelli, A.N.C. Neto, O.L. Malta, *J. Lumin.* **131** (2011) 1026–1028.
[34] E.J. Little, Jr., M.M. Jones, *J. Chem. Educ.* **37** (1960) 231–233.
[35] R.D. Shannon, *Acta Cryst. A.* **32** (1976) 751–767.
[36] F. Izumi, K. Momma, *Solid State Phenom.* **130** (2007) 15–20.
[37] K.R. Whittle, G.R. Lumpkin, F.J. Berry, G. Oates, K.L. Smith, S. Yudintsev, N.J. Zaluzec, *J. Solid State Chem.* **180** (2007) 785–791.
[38] D. Waasmaier and A. Kirfel, *Acta Crystallogr.* **A51** (1995) 416–431.
[39] M. Hietaniemi, T. Hu, J. Välikangas, J. Niittykoski, U. Lassi, *J. Appl. Electrochem.* 51 (2021) 1545–1557.
[40] M. Nie, Y.-F. Xia, Z.-B. Wang, Y. Fuda, Y. Zhang, W. Jin, W. Bing, *Ceram. Int.* **41** (2015) 15185–15192.
[41] Z. Chen, J. Wang, D. Chao, T. Baikie, L. Bai, S. Chen, Y. Zhao, T.C. Sum, J. Lin, Z. Shen, *Sci. Rep.* **6** (2016) 25771.
[42] A.K. Singh, S. Chauhan, S.K. Srivastava, R. Chandra, *Solid State Commun.* **242** (2016) 74–78.
[43] M.G. Brik, Ž.M. Antić, K. Vuković, M.D. Dramićanin, *Mater. Trans.* **56** (2015) 1416–1418.
[44] A.V. Egorysheva, V.D. Volodin, A.A. Chistyakov, Y.A. Kuzishchin, V.M. Skorikov, T.D. Dudkina, *Inorg. Mater.* **46** (2010) 1384–1390.
[45] Y. Li, N. Li, P. Zhang, Z. Wei, Z. Wang, L. Zhao, W. Chen, D Spectrochim. *Acta A Mol. Biomol. Spectrosc.* **248** (2021) 119247.
[46] R. Skaudzius, A. Katelnikovas, D. Enseling, A. Kareiva, T. Jüstel, *J. Lumin.* **147** (2014) 290–294.
[47] A. Nakatsuka, A. Yoshiasa, T. Yamanaka, *Acta Crystallogr.* **B55** (1999) 266–272.
[48] A. Nakatsuka, A. Yoshiasa, S. Takeno, *Acta Crystallogr.* **B51** (1995) 737–745.

Chapter 3

Effect of A-site deficiency on perovskite-type Mn^{4+}-activated $La_{5/3}MgTaO_6$ red phosphor and green luminescence of the Mn^{2+} occupied six-coordinate site in Mg_2LaTaO_6

3.1 Introduction

White LEDs are used worldwide owing to their energy efficiency, high luminous intensity, and long operational life [1–3]. These comprise blue LEDs [4] with yellow phosphors ($Y_3Al_5O_{12}:Ce^{3+}$) [5]. These colors are complementary and thus produce white light; however, white LEDs also exhibit low color rendering owing to the lack of a red component, which limits their applications [6]. Red phosphors excited by ultraviolet (UV) and blue light have been developed to solve this problem [7], and the resulting high-color-rendering white LEDs enable control of the color tone of lighting and are expected to have a wide range of applications.

Certain Eu-activated red phosphors, including $CaAlSiN_3:Eu^{2+}$ and $M_2Si_5N_8:Eu^{2+}$ (M = Ca, Sr, Ba), have been synthesized for practical use [8,9]; however, Eu is expensive, and such devices are not widely available because their production is unevenly distributed around the world.

Herein, we develop Mn-activated phosphors as an alternative to Eu-activated red phosphors. Mn^{4+}-activated phosphors are known to absorb near-UV light and emit red light. Moreover, Mn is considerably cheaper than Eu [10–13]. Mn-activated phosphors have recently attracted considerable attention as promising red phosphor candidates for use in high-color-rendering white LEDs, such as $NaLaMgWO_6:Mn^{4+}$ [10], $Sr_2Ca_{1-\delta}Ln_\delta WO_6:Mn^{4+}$ [11], $Sr_3LiSbO_6:Mn^{4+}$ [12], $Sr_2ScO_3F:Mn^{4+}$ [13].

Despite their potential as red phosphors, the absorption and emission of Mn^{4+} are typically assigned to forbidden transitions. Mn^{4+} preferentially occupies six-coordinate octahedral sites with a center of inversion [14]; however, a high luminescence efficiency is not achieved from the octahedral Mn^{4+} owing to its selectivity as per the Laporte rule [15]. To solve this problem, we selected $La_{5/3}MgTaO_6$ as a host material for

the Mn^{4+} activators. The crystal structure of $La_{5/3}MgTaO_6$ is characterized by a double perovskite-type structure with a regular deficiency of La^{3+} along the c-axis [16] (Fig. 3.1). $La_{5/3}MgTaO_6$ contains [TaO_6] octahedra, which facilitates the entry of Mn^{4+} ions into the six-coordinate octahedral sites. The Mn^{4+} in the B-site of the perovskite-type structure is thus displaced, thereby removing the center of inversion from $La_{5/3}MgTaO_6$. For example, in the defect-perovskite structures of lithium-containing lanthanum metaniobates and metatantalates, the cation at the B-site is displaced toward the deficient A-site as the amount of lithium is decreased [17]. Based on these observations, we predict that the Mn^{4+}-activated $La_{5/3}MgTaO_6$ phosphor will exhibit high-intensity red emission owing to the loss of the inversion symmetry center. A Mn^{4+}-activated $SrLa_2Mg_2W_2O_{12}$ red phosphor with A-site deficiency in the structure and high luminescence was recently reported by Shi et al [18]; however, the relationship between A-site deficiency and luminescence in the perovskite-type structure has not yet been reported. Zhou et al. synthesized the perovskite-type $BaLaMgTaO_6$:Mn^{4+} red phosphor via a high-temperature solid-state procedure [19], the final calcination temperature (1500 °C) and reaction time (6 h) of which are identical to those used in the synthesis of $La_{5/3}MgTaO_6$ [16]. In addition, the ionic radius of Ba^{2+} (1.42 Å (eight-coordination)) is similar to that of La^{3+} (1.160 Å (eight-coordination)), making Ba^{2+} a suitable dopant for the La^{3+} sites [20]. In this study, we synthesized the Mn^{4+}-activated phosphors, $La_{5/3-(2/3)x}Ba_xMgTa_{0.99}O_6$:$0.01Mn^{4+}$ (x = 0, 0.2, 0.4, 0.6, 0.8, and 1) at 1500 °C for 6 h. By substituting Ba^{2+} into the A site of $La_{5/3}MgTaO_6$, we investigated the relationship between the A-site deficiency and the luminescence properties of the material.

We also synthesized the Mn-activated phosphors, $La_{5/3-(2/3)y}Mg_{1+y}Ta_{0.99}O_6$:0.01Mn ($y$ = 0, 0.2, 0.4, 0.6, 0.8, and 1), and investigated the effect of

increasing *y* on their crystal structure evolution and luminescence properties. With a *y* value of 1, the chemical composition of this phosphor is represented as Mg_2LaTaO_6, which has an oxide ion-deficient pyrochlore-type structure [21]. Mn^{4+}-activated pyrochlore-type $RE_2Sn_2O_7$ ($RE^{3+} = Y^{3+}$, Lu^{3+} or Gd^{3+}) phosphors were previously shown to exhibit red luminescence [22]. To the best of our knowledge, all Mn-activated pyrochlore-type phosphors emit red light. Inspired by this, we synthesized the first Mn-activated pyrochlore-type Mg_2LaTaO_6 phosphor.

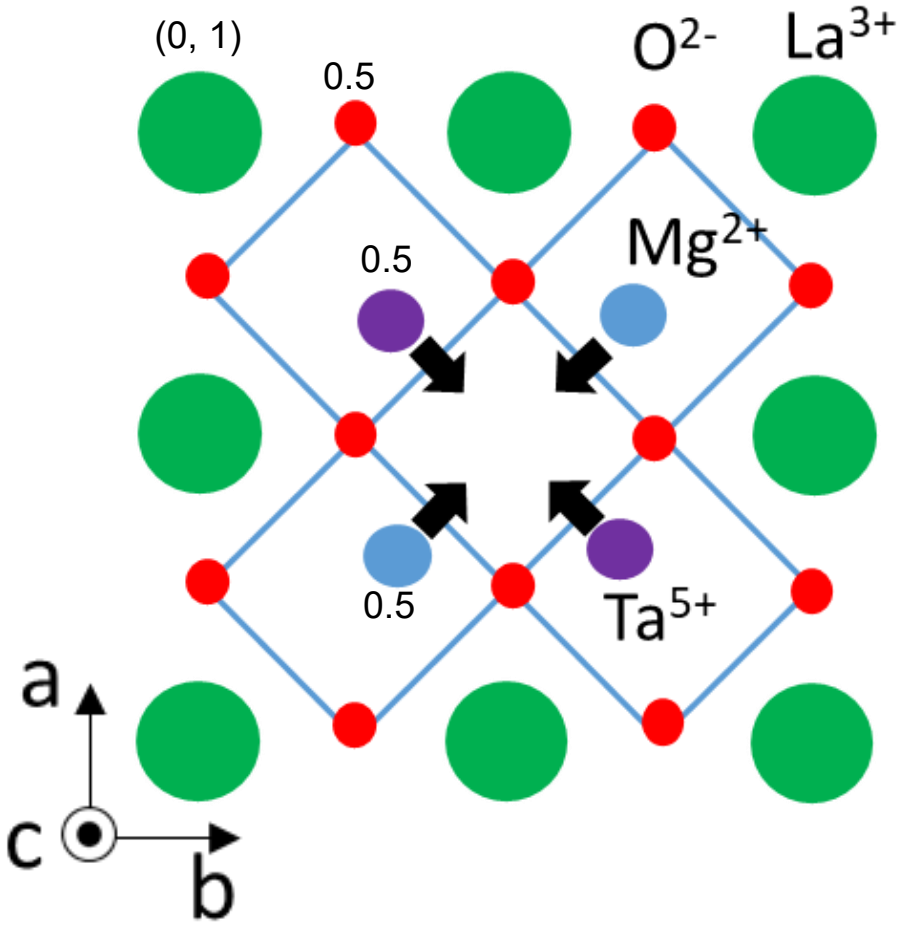

Fig. 3.1 Crystal structure of $La_{5/3}MgTaO_6$. La^{3+} in the center is missing. Mg^{2+} and Ta^{5+} ions may be shifted along the respective arrows.

3.2 Sample synthesis

$La_{5/3-(2/3)x}Ba_xMgTa_{0.99}Mn_{0.01}O_6$ (x = 0, 0.2, 0.4, 0.6, 0.8, and 1) and $La_{5/3-(2/3)y}Mg_{1+y}Ta_{0.99}Mn_{0.01}O_6$ (y = 0, 0.2, 0.4, 0.6, 0.8, and 1) phosphors were synthesized by a solid-state reaction. The Mn doping level was fixed at 1% of Ta. Stoichiometric amounts of La_2O_3 (99.9%, Kojundo Chemical, Japan), $4MgCO_3 \cdot Mg(OH)_2 \cdot 5H_2O$ (485.65 g/mol, Kishida Chemical, Japan), Ta_2O_5 (99.95%, Kanto Chemical, Japan), $MnCO_3$ (99.9%, Kojundo Chemical, Japan), and $BaCO_3$ (99.9%, Kanto Chemical, Japan) were ground and mixed in an agate mortar for 40 min. After calcination at 1200 °C for 4 h, the mixture was cooled to room temperature and thereafter mixed for a further 20 min. Finally, the mixture was calcined at 1500 °C for 6 h to obtain the desired products.

3.3 Characterization

The crystalline structures of the phosphors were investigated at room temperature using powder X-ray diffraction (XRD, SmartLab X-ray Diffractometer, Rigaku, Japan) with Cu-Kα radiation at 45 kV, 200 mA, and 2θ in the range of 10–60°. The particle shape and size were determined using scanning electron microscopy (SEM, JSM-6510A, JEOL, Japan). The luminescence properties of all the phosphors were measured using fluorescence spectrometry (FP-8300 Spectrofluorometer, JASCO, Japan). Phosphors of the same amount (weighted 0.150 g) were used for comparison with the same holder. The X-ray absorption near edge structure (XANES) spectrum of the Mn-K edge in fluorescent mode was measured using the BI16B2 beamline at SPring-8, Japan. X-ray energy selection was achieved using a silicon (111) double crystal monochromator. A 25-element solid-state detector (25-element SSD) was used owing to the low concentration of Mn. A Cr metal foil was set in front of the SSD for band-pass filter. The XANES spectra were measured at a rate of 45 (x, y = 1 samples) and 54 (x = 0 sample) seconds per point, respectively. After the XANES measurement, the background process was conducted using the REX2000 software.

3.4 Results and Discussion

3.4.1 $La_{5/3-(2/3)x}Ba_xMgTa_{0.99}Mn_{0.01}O_6$ (x = 0, 0.2, 0.4, 0.6, 0.8, and 1) phosphors

XRD patterns

The XRD patterns of $La_{5/3-(2/3)x}Ba_xMgTa_{0.99}Mn_{0.01}O_6$ (x = 0, 0.2, 0.4, 0.6, 0.8, and 1) phosphors calcined at 1500 °C for 6 h are shown in Fig. 3.2. The diffraction patterns of the samples with x = 0 and 1 are consistent with the Joint Committee on Powder Diffraction Standards (JCPDS) card peak patterns of $La_{5/3}MgTaO_6$ [16] and $BaLaMgTaO_6$ [23], respectively, confirming the formation of single-phase phosphors. The patterns of samples with x = 0.2–0.8 did not exhibit any peaks corresponding to other phases. The peak at ~32° continuously shifted to a lower angle with increasing x, indicating that Ba was successfully doped into the perovskite-type structure (Fig. 3.2, right side).

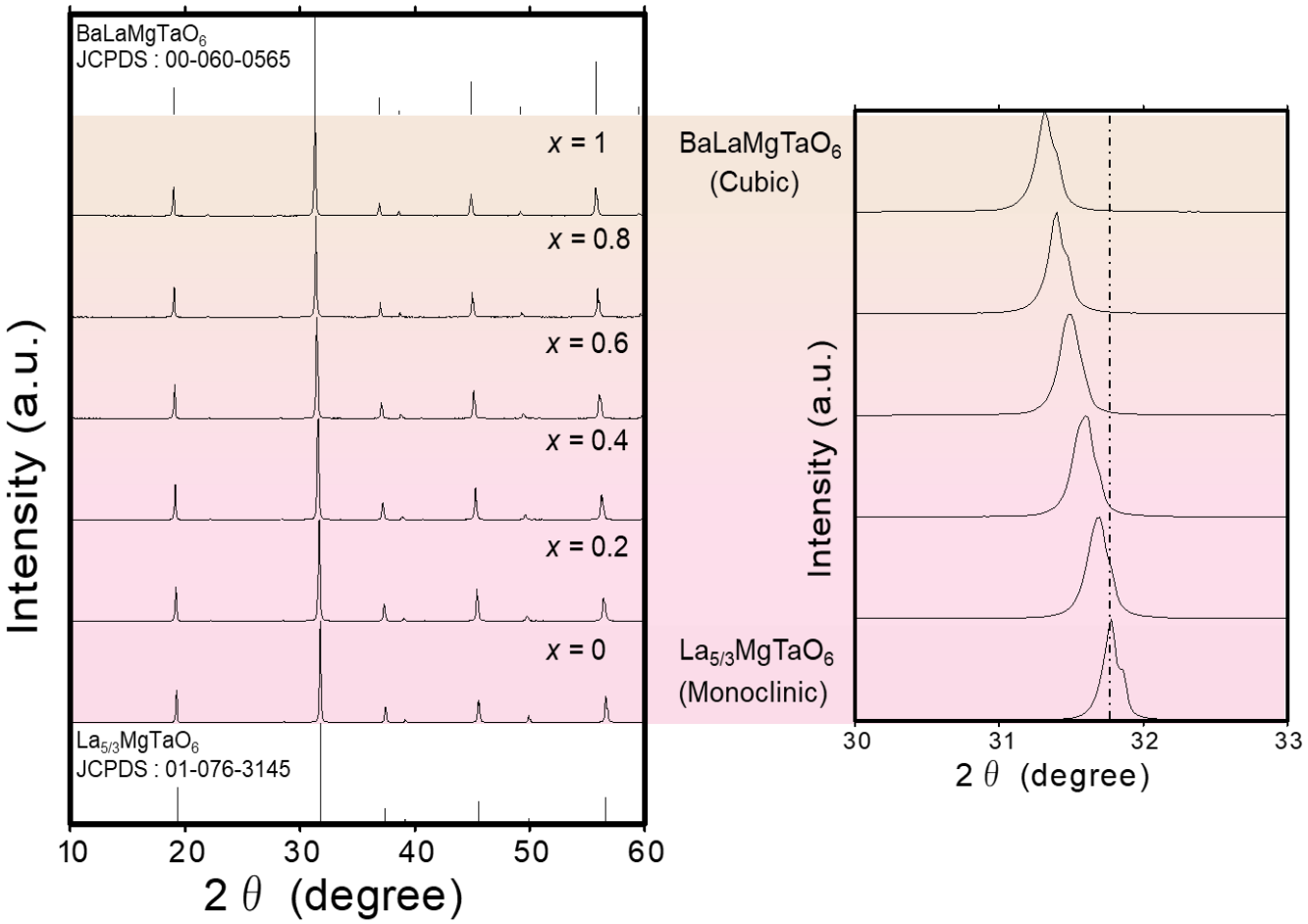

Fig. 3.2 XRD patterns of $La_{5/3-(2/3)x}Ba_xMgTa_{0.99}O_6:0.01Mn^{4+}$ (x = 0, 0.2, 0.4, 0.6, 0.8, and 1).

SEM image

SEM images of Mn^{4+}-activated $La_{5/3}MgTaO_6$ ($x = 0$) and $BaLaMgTaO_6$ ($x = 1$) phosphors are shown in Fig. 3.3(a) and (b), respectively. We observed coarse particles measuring ~10–20 micrometers and fine particles measuring several micrometers.

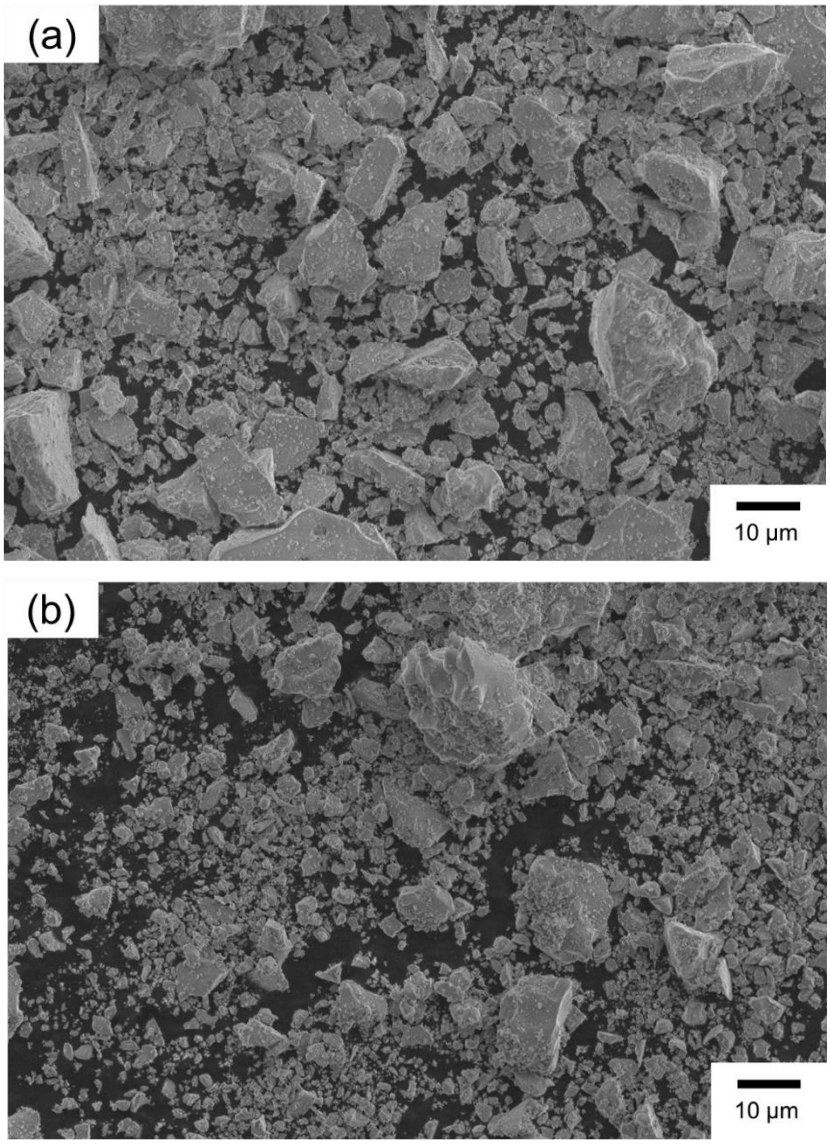

Fig. 3.3 SEM images of Mn^{4+}-activated (a) $La_{5/3}MgTaO_6$ ($x = 0$) and (b) $BaLaMgTaO_6$ ($x = 1$) phosphors.

PL measurement

The excitation and emission spectra of $La_{5/3-(2/3)x}Ba_xMgTa_{0.99}Mn_{0.01}O_6$ (x = 0, 0.2, 0.4, 0.6, 0.8, and 1) phosphors are shown in Fig. 3.4(a) and Fig. 3.4(b), respectively. The excitation spectra showed an absorption maximum at ~365 nm, while the fluorescence spectra showed red emission with a maximum at ~706 nm. The sample with x = 0 exhibited the strongest absorption of UV light and emission of red light at ~365 and 706 nm, respectively, demonstrating its potential as a phosphor for high-color-rendering white LEDs by applying near-UV light excitation. As the amount of Ba^{2+} substitution increased, both the absorption and emission intensities tended to decrease.

Images of $La_{5/3-(2/3)x}Ba_xMgTa_{0.99}Mn_{0.01}O_6$ (x = 0, 0.2, 0.4, 0.6, 0.8, and 1) phosphors under UV excitation of 365 nm (Fig. 3.5) show that the red luminescence tends to be quenched with increasing x. The sample with x = 0 exhibited the strongest red emission. We hypothesize that the center of inversion in $La_{5/3}MgTaO_6$, was lost owing to the displacement of Mn^{4+} occupying the B-site toward the deficient A-site to avoid electrostatic repulsion. Accordingly, the forbidden transition was relaxed in the x = 0 sample. In addition, the luminescence tended to be increasingly quenched with increasing x, indicating that reducing the A-site deficiency by the substitution of Ba^{2+} revives the center of inversion (Fig. 3.6).

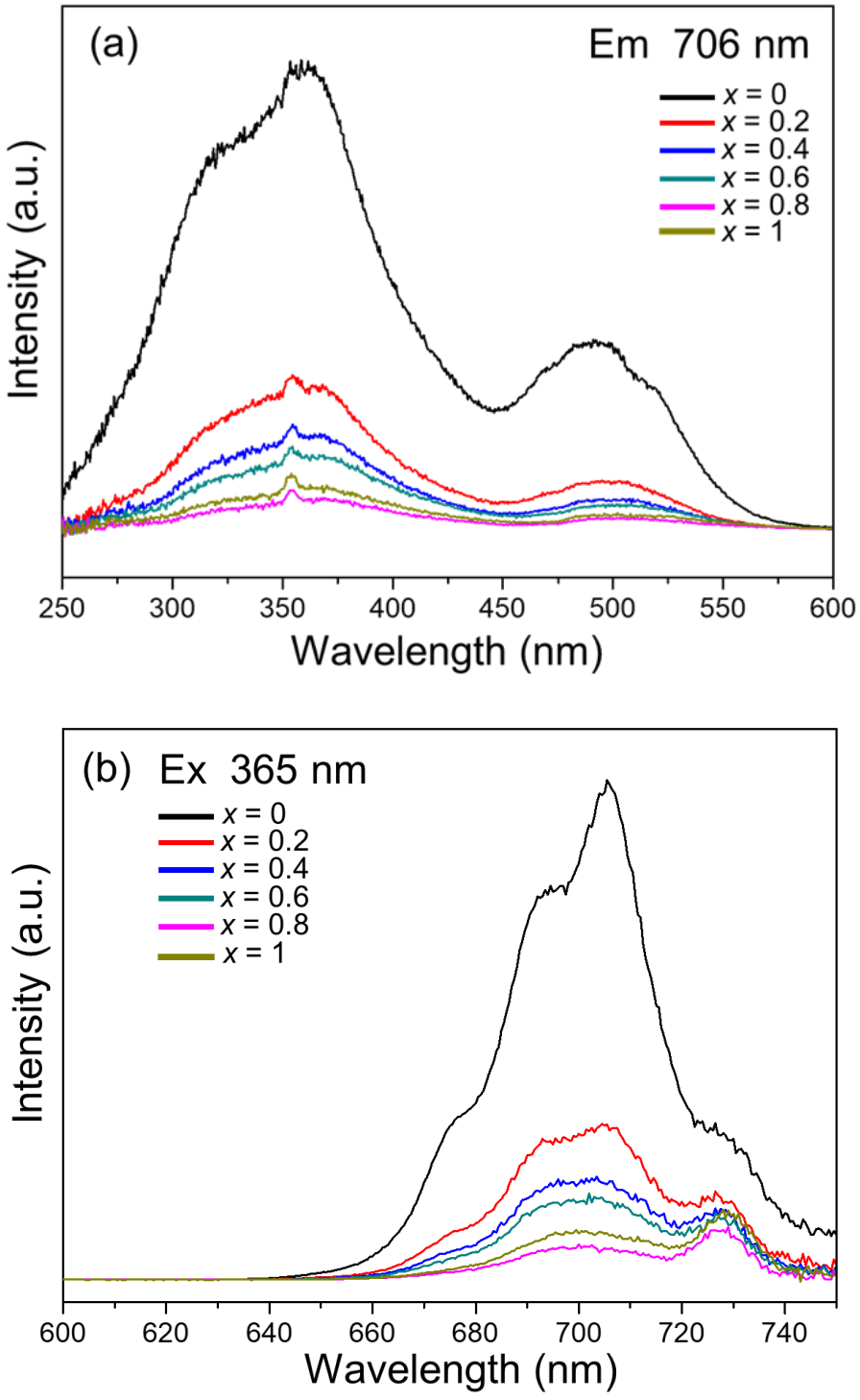

Fig. 3.4 (a) Excitation and (b) emission spectra of $La_{5/3-(2/3)x}Ba_xMgTa_{0.99}O_6:0.01Mn^{4+}$ (x = 0, 0.2, 0.4, 0.6, 0.8, and 1).

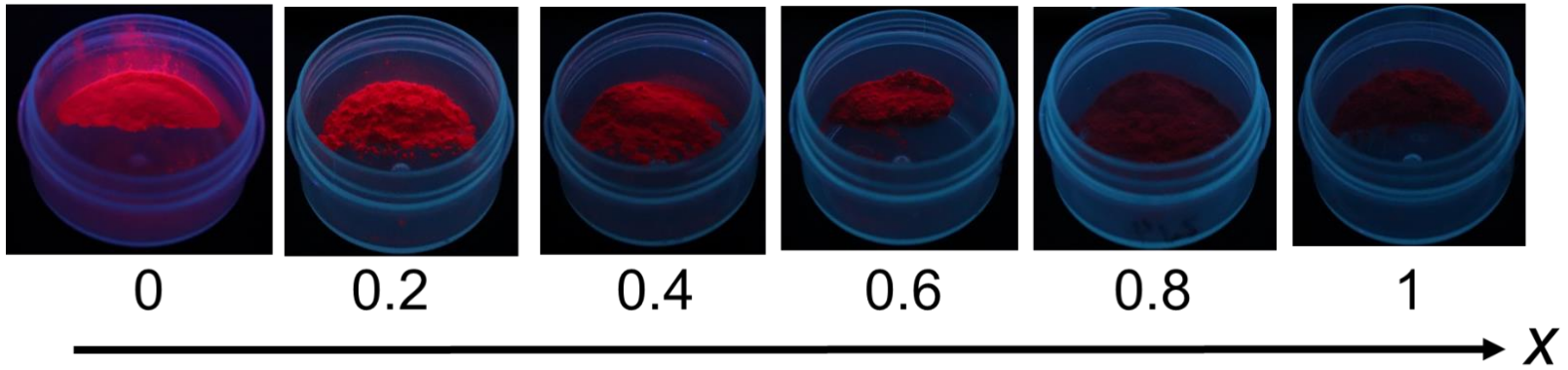

Fig. 3.5 Photographs of $La_{5/3-(2/3)x}Ba_xMgTa_{0.99}O_6:0.01Mn^{4+}$ (x = 0, 0.2, 0.4, 0.6, 0.8, and 1) under UV excitation at 365 nm.

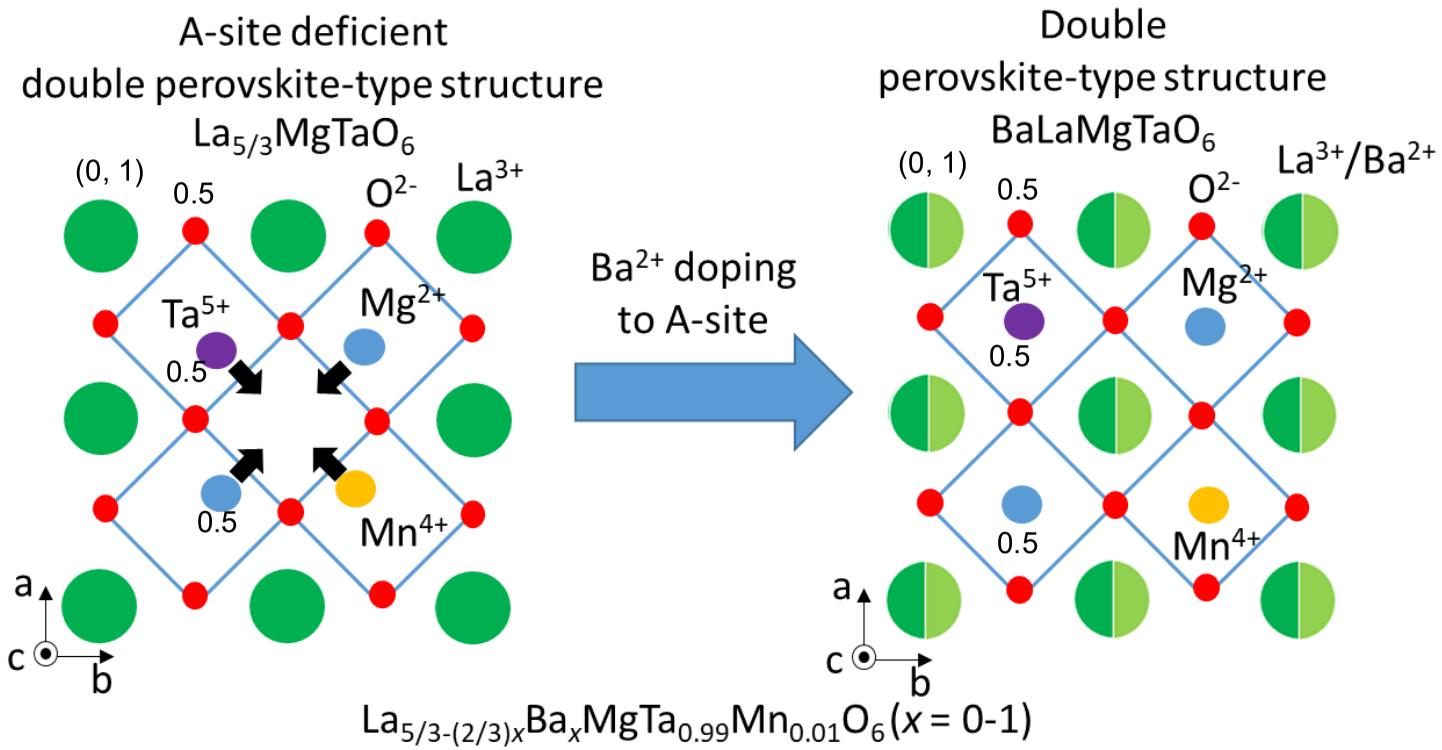

Fig. 3.6 Crystal structure of $La_{5/3}MgTaO_6$ (left) and $BaLaMgTaO_6$ (right). The A-site cation deficiency in $La_{5/3}MgTaO_6$ decreases with increasing x. The B-site cation is displaced in the direction of A-site deficiency to avoid electrostatic repulsion with the A-site cation La^{3+}. ion at 365 nm.

XANES measurement of

XANES is an effective technique to probe the local coordination environment at a particular location in the structure. Yamamoto introduced the importance of the intensity of the pre-edge peak in terms of the d-p hybridization, which is dominated by the orbital symmetry and can be explained by group theory. The formation of the d-p hybridized orbital results in an intense pre-edge peak owing to the mixing of s-p electric dipole transitions [24]. Farges reported that the intensity of the pre-edge peak at ~6540 eV in the Mn K-edge XANES spectrum increased as the symmetry around the Mn^{2+} center was reduced [25].

The Mn K-edge XANES spectra of $La_{5/3}MgTa_{0.99}Mn_{0.01}O_6$ (x = 0) and $BaLaMgTa_{0.99}Mn_{0.01}O_6$ (x = 1) phosphors are shown in Fig. 3.7. A low-intensity pre-edge peak was observed at approximately 6540–6545 eV in A-site deficient perovskite-type structure. Therefore, this result provides evidence that Mn^{4+} occupies the non-inversion center and explains the strong red emission of the A-site deficient perovskite-type structure.

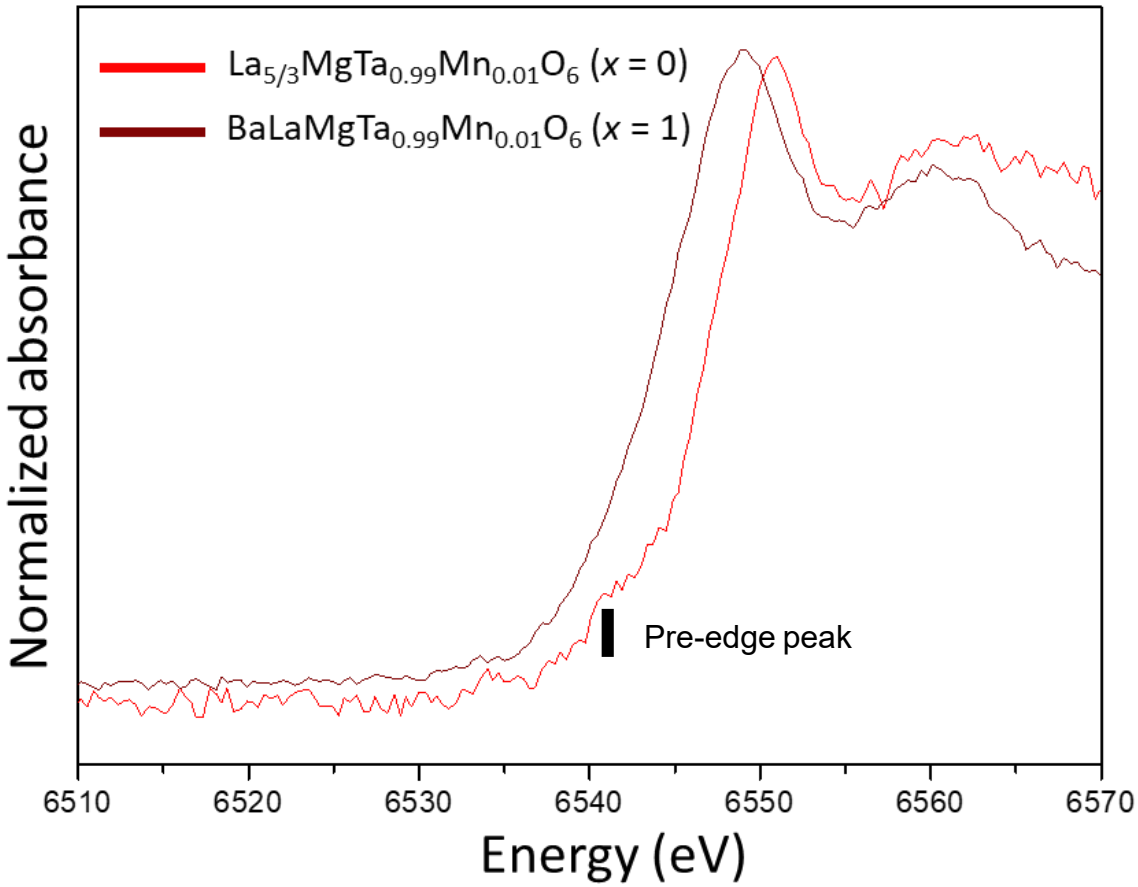

Fig. 3.7 Mn- K edge normalized XANES spectra of $La_{5/3}MgTa_{0.99}Mn_{0.01}O_6$ and $BaLaMgTa_{0.99}Mn_{0.01}O_6$ phosphors.

3.4.2 $La_{5/3-(2/3)y}Mg_{1+y}Ta_{0.99}O_6$:0.01Mn ($y$ = 0, 0.2, 0.4, 0.6, 0.8, and 1) phosphors

XRD patterns

The XRD patterns of the $La_{5/3-(2/3)y}Mg_{1+y}Ta_{0.99}Mn_{0.01}O_6$ (y = 0, 0.2, 0.4, 0.6, 0.8, and 1) phosphors calcined at 1500 °C for 6 h are shown in Fig. 3.8. The pattern of the sample with y = 0 matched the peak pattern of $La_{5/3}MgTaO_6$, confirming the single-phase phosphor. In contrast, a new diffraction peak appeared at ~29° as y increased. These star-shaped peaks are derived from the oxide ion-deficient pyrochlore-type structure of Mg_2LaTaO_6 [21]. A small amount of MgO was also detected as a byproduct in samples with y = 0.2–1. Magnification of the strongest diffraction peaks at ~27°–33° shows that the peak shift was not significant. With an increase in y, the intensity of the peaks derived from $La_{5/3}MgTaO_6$ decreased and that derived from Mg_2LaTaO_6 increased. This result demonstrates that the addition of Mg to La does not form a solid solution in the perovskite-type $La_{5/3}MgTaO_6$ structure.

The perovskite-type structure was retained in $La_{5/3-(2/3)x}Ba_xMgTa_{0.99}Mn_{0.01}O_6$ (x = 0, 0.2, 0.4, 0.6, 0.8, and 1) regardless of the x value; however, $La_{5/3-(2/3)y}Mg_{1+y}Ta_{0.99}Mn_{0.01}O_6$ (y = 0, 0.2, 0.4, 0.6, 0.8, and 1) formed a pyrochlore-type structure as y increased. This result was attributed to the difference in the ionic radii of Mg^{2+} and Ba^{2+} used as the dopants. Because the ionic radius of Ba^{2+} (1.42 Å (eight-coordination)) is larger than that of Mg^{2+} (0.89 Å (eight-coordination)) [20], the perovskite-type structure, wherein the A-site cation prefers a greater coordination number, is stabilized in the $La_{5/3-(2/3)x}Ba_xMgTa_{0.99}Mn_{0.01}O_6$ (x = 0, 0.2, 0.4, 0.6, 0.8, and 1) system.

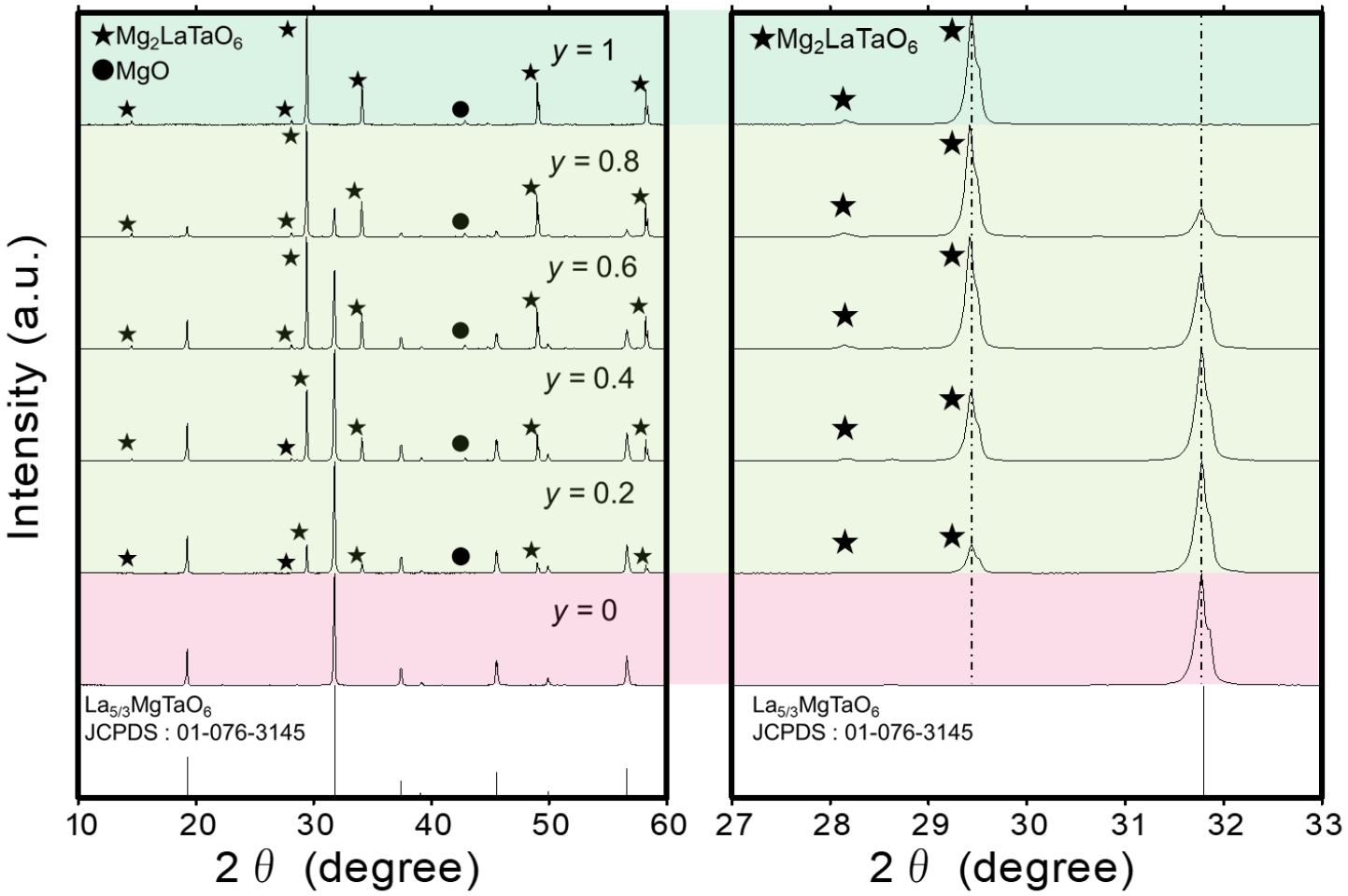

Fig. 3.8 XRD patterns of $La_{5/3-(2/3)y}Mg_{1+y}Ta_{0.99}O_6$:0.01Mn ($y$ = 0, 0.2, 0.4, 0.6, 0.8, and 1).

SEM image

A SEM image of the Mn-activated Mg_2LaTaO_6 (y = 1) phosphor is shown in Fig. 3.9. The particle size of this phosphor was several micrometers, and the particles were smoother and more uniform than those of the Mn^{4+}-activated perovskite-type phosphors.

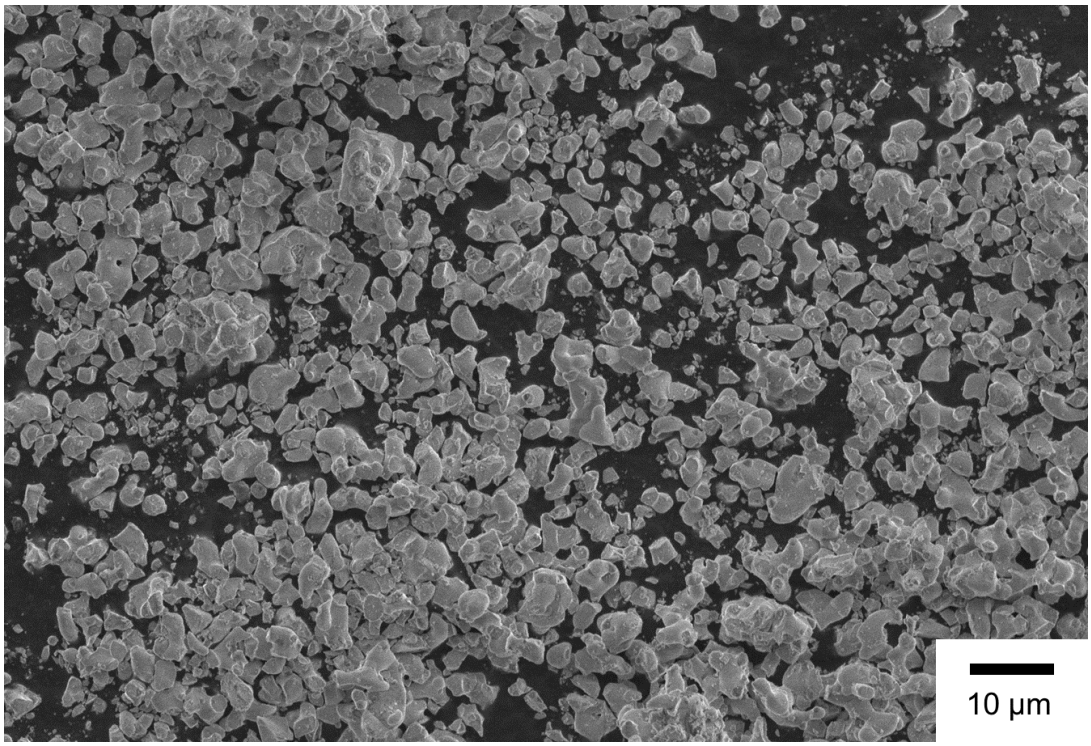

Fig. 3.9 SEM image of Mn-activated Mg_2LaTaO_6 (y = 1) phosphor.

PL measurement

The emission spectra of $La_{5/3-(2/3)y}Mg_{1+y}Ta_{0.99}Mn_{0.01}O_6$ (y = 0, 0.2, 0.4, 0.6, and 0.8) phosphors excited at 365 nm are shown in Fig. 3.10. As y increased, the emission intensity tended to decrease.

Images of $La_{5/3-(2/3)y}Mg_{1+y}Ta_{0.99}Mn_{0.01}O_6$ (y = 0, 0.2, 0.4, 0.6, 0.8, and 1) phosphors under UV excitation at 365 nm are shown in Fig. 3.11. The quenching of red luminescence tends to increase with increasing y. The XRD patterns revealed that the extent of the $La_{5/3}MgTaO_6$ phase decreased with increasing y value (Fig. 3.8); therefore, the decreasing trend in the emission intensity is caused by a reduction in the amount of the $La_{5/3}MgTaO_6$ phase that emits red light.

The excitation spectra of $La_{5/3-(2/3)y}Mg_{1+y}Ta_{0.99}Mn_{0.01}O_6$ (y = 0.2, 0.4, 0.6, 0.8, and 1) phosphors at 540 nm showed absorption maxima at ~254 nm (Fig. 3.12(a)), while the fluorescence emission spectrum showed green emission with a maximum at ~540 nm (Fig. 3.12(b)). The intensity of this green emission increased as y increased, suggesting that the amount of the pyrochlore-type Mg_2LaTaO_6 phase, which emits green light, increases with increasing y, whereas the amount of the perovskite-type $La_{5/3}MgTaO_6$ phase, which emits red light, decreases.

Images of $La_{5/3-(2/3)y}Mg_{1+y}Ta_{0.99}Mn_{0.01}O_6$ (y = 0, 0.2, 0.4, 0.6, 0.8, and 1) phosphors under UV 254 nm are shown in Fig. 3.13. The sample with y = 0 consisted of a single phase of $La_{5/3}MgTaO_6$: thus, the red luminescence must be derived from the perovskite-type $La_{5/3}MgTaO_6$. In contrast, the sample with y = 1 primarily contained the Mg_2LaTaO_6 phase, demonstrating that the green luminescence was derived from the pyrochlore-type Mg_2LaTaO_6. Orange/yellow emissions were observed from samples with y = 0.4 and 0.6 owing to the mixture of the perovskite-type red phosphor and

pyrochlore-type green phosphor in the samples with y = 0.2 to 0.8.

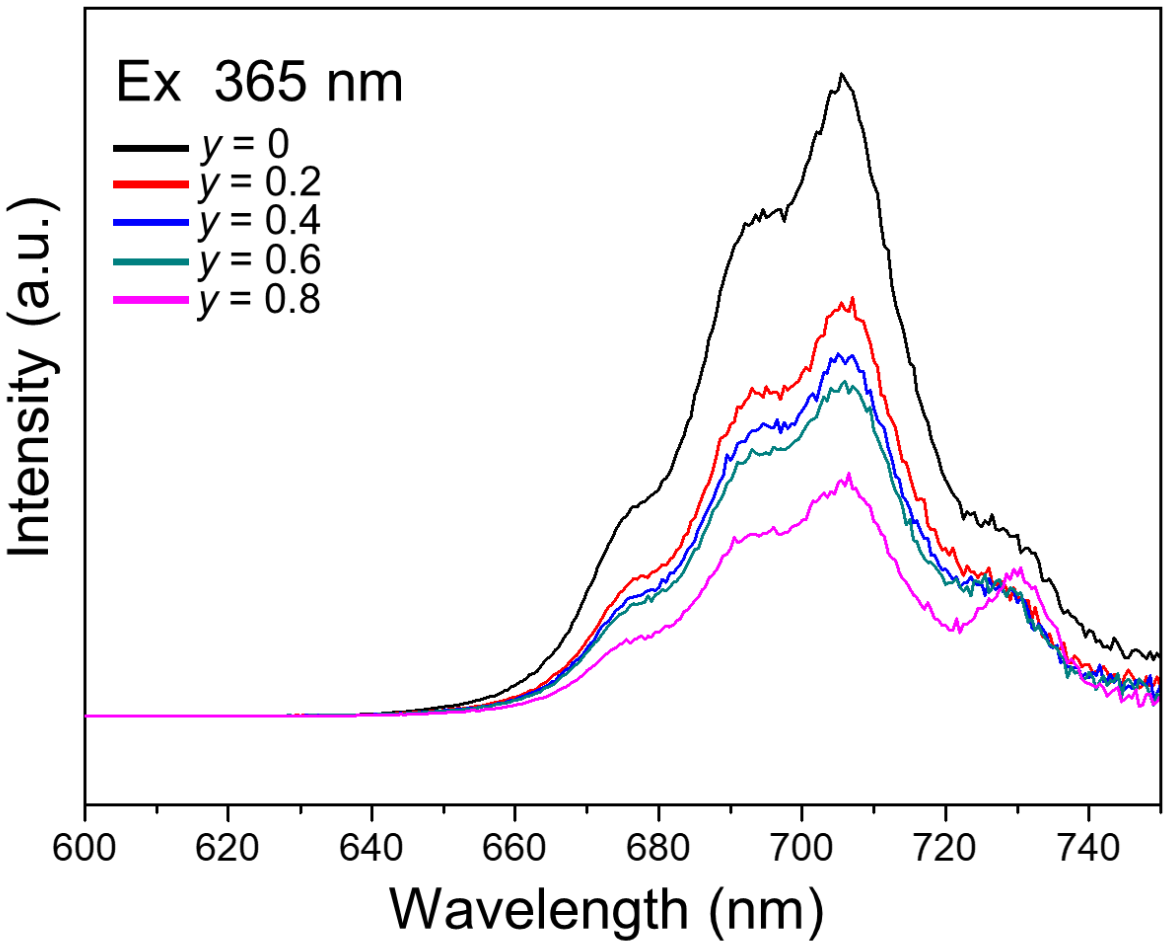

Fig. 3.10 Emission spectra of $La_{5/3-(2/3)y}Mg_{1+y}Ta_{0.99}O_6$:0.01Mn ($y$ = 0, 0.2, 0.4, 0.6, and 0.8).

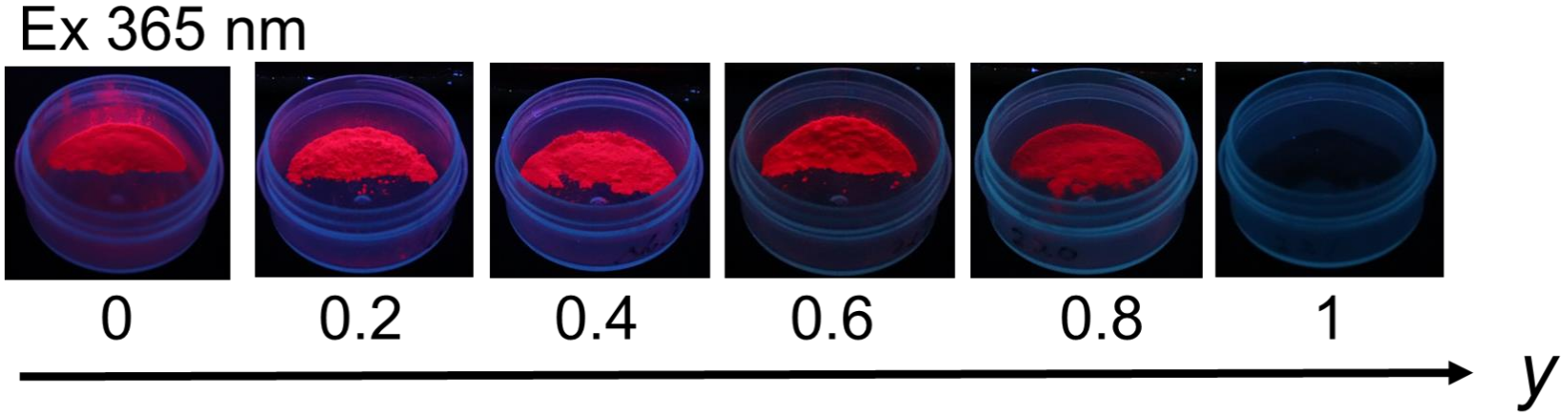

Fig. 3.11 Photographs of $La_{5/3-(2/3)y}Mg_{1+y}Ta_{0.99}O_6$:0.01Mn ($y$ = 0, 0.2, 0.4, 0.6, 0.8, and 1) under UV excitation at 365 nm.

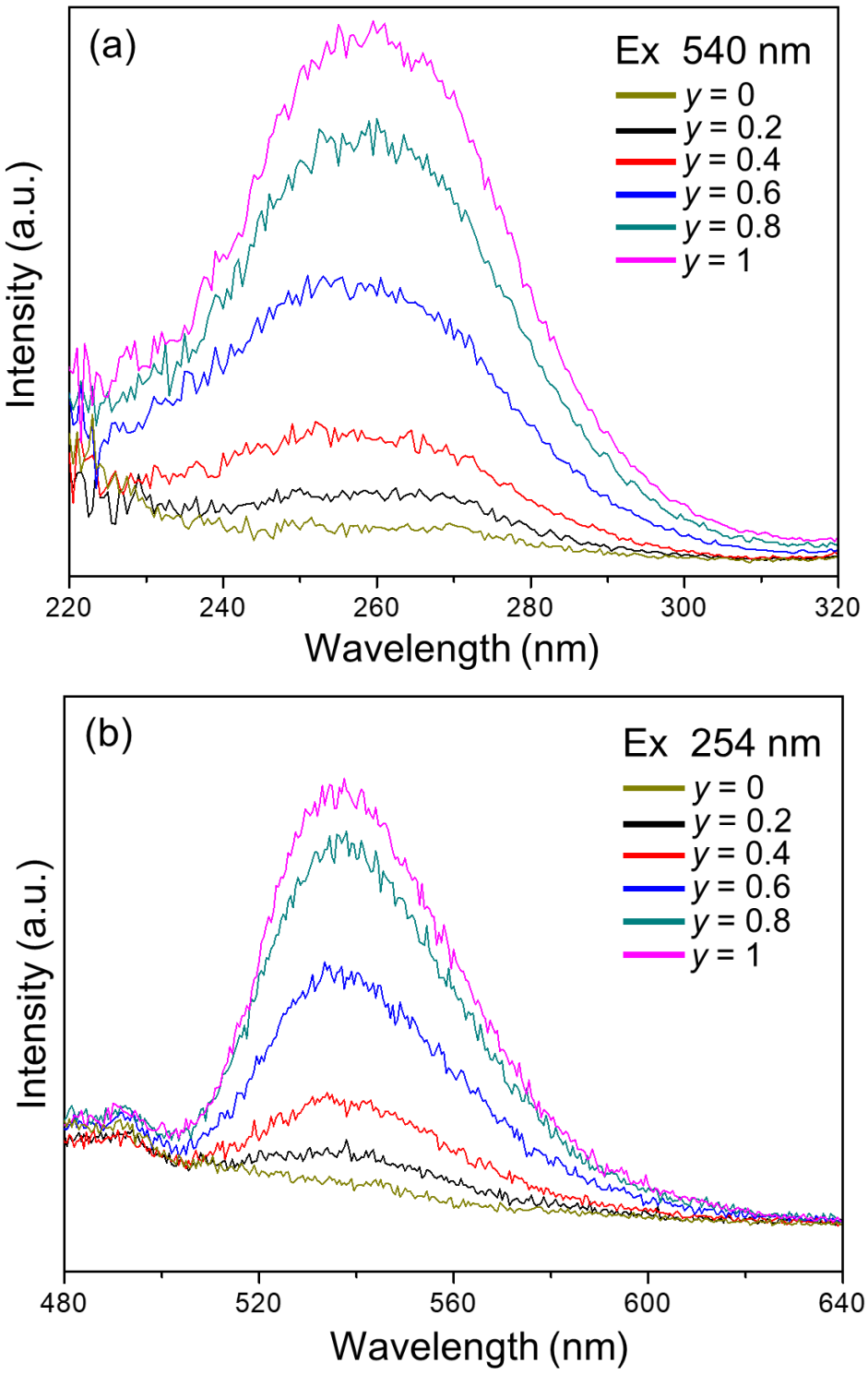

Fig. 3.12 (a) Excitation and (b) emission spectra of $La_{5/3-(2/3)x}Mg_{1+y}Ta_{0.99}O_6:0.01Mn^{2+}$ (y = 0, 0.2, 0.4, 0.6, 0.8, and 1).

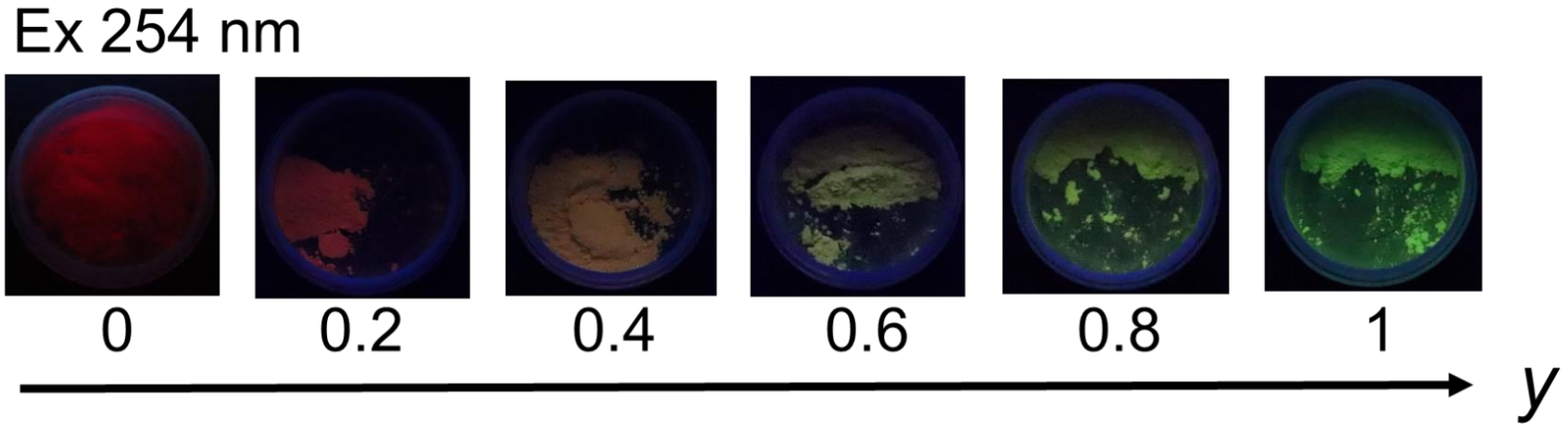

Fig. 3.13 Photographs of $La_{5/3-(2/3)y}Mg_{1+y}Ta_{0.99}O_6$:0.01Mn ($y$ = 0, 0.2, 0.4, 0.6, 0.8, and 1) under UV excitation at 254 nm.

Local coordination environment around Mn in pyrochlore-type Mg_2LaTaO_6

The local coordination environment of pyrochlore-type Mg_2LaTaO_6 was explored, and a schematic of its structure was produced (Fig. 3.14). The composition of the ideal pyrochlore-type structure is expressed as $A_2B_2X_7$, in which the A-cation occupies the 16d site (eight-coordinate site), and the B-cation occupies the 16c site (six-coordinate site) [26]. The X anions occupy the 48f and 8b sites, while the 8a site is unoccupied. Kumar et al. [21] found that Mg and La were randomly distributed across the 16d sites (A-site) in oxide-ion deficient pyrochlore-type Mg_2LaTaO_6, while Mg and Ta were randomly distributed across the 16c sites (B-site). The sum of the bond strengths of the 48f sites and 8b sites in Mg_2LaTaO_6 is calculated by Pauling's second law [27], as shown in Fig. 3.15. The sum of the bond strengths of the 48f position is closer to -2 than that of the 8b position, suggesting that oxide ions are preferentially lost from the 8b. Accordingly, this deficient pyrochlore-type Mg_2LaTaO_6 structure consists of AO_6 and BO_6 octahedra owing to the empty 8b sites. Both AO_6 and BO_6 octahedra have a center of inversion identical to that of the nominal pyrochlore-type structure. Ramesha et al. reported an oxygen ion-deficient pyrochlore-type Pb_2MnReO_6 [28]. Their refinement demonstrated that Mn^{2+} and Re^{6+} are disordered at 16c sites, while the O^{2-} anions occupied the 48f sites and the 8b site was unoccupied. The crystal structure of Pb_2MnReO_6 is shown in Fig. 3.16. The BO_6 polyhedra in Pb_2MnReO_6 were highly distorted in a similar way to the highly distorted BO_6 octahedron found in Mg_2LaTaO_6 [21].

The coordination environment in the vicinity of Mn was evaluated using XANES. The Mn K-edge XANES spectrum of $Mg_2LaTa_{0.99}Mn_{0.01}O_6$ ($y = 1$) phosphor is shown in Fig. 3.17. The pre-edge peak was not identified in the spectrum of the

pyrochlore-type Mg_2LaTaO_6 phosphor, leading us to conclude that Mn occupied the site with a center of inversion.

Mn^{4+} phosphors emit red light regardless of the parent material [10–13]; however, the emission wavelength of Mn^{2+}-activated phosphors is dependent on the crystal field. As the crystal field becomes stronger, the emission wavelength shifts toward longer wavelengths. For example, in the case of the oxide phosphor, Mn^{2+} in a four-coordinate site without a center of inversion exhibits green emission owing to the relatively weak crystal field, while that in a six-coordinate site emits orange/red light as a result of the stronger crystal field [30–33].

Table 3.1 shows the emission wavelengths and coordination numbers of the Mn^{2+} oxide phosphors [30–40]. The Mn-activated Mg_2LaTaO_6 phosphors, in which the six-coordinate sites are occupied, exhibited an emission peak at an intermediate wavelength (540 nm), suggesting that the highly distorted BO_6 octahedron may weaken the crystal field, thus resulting in green emission from Mn^{2+}.

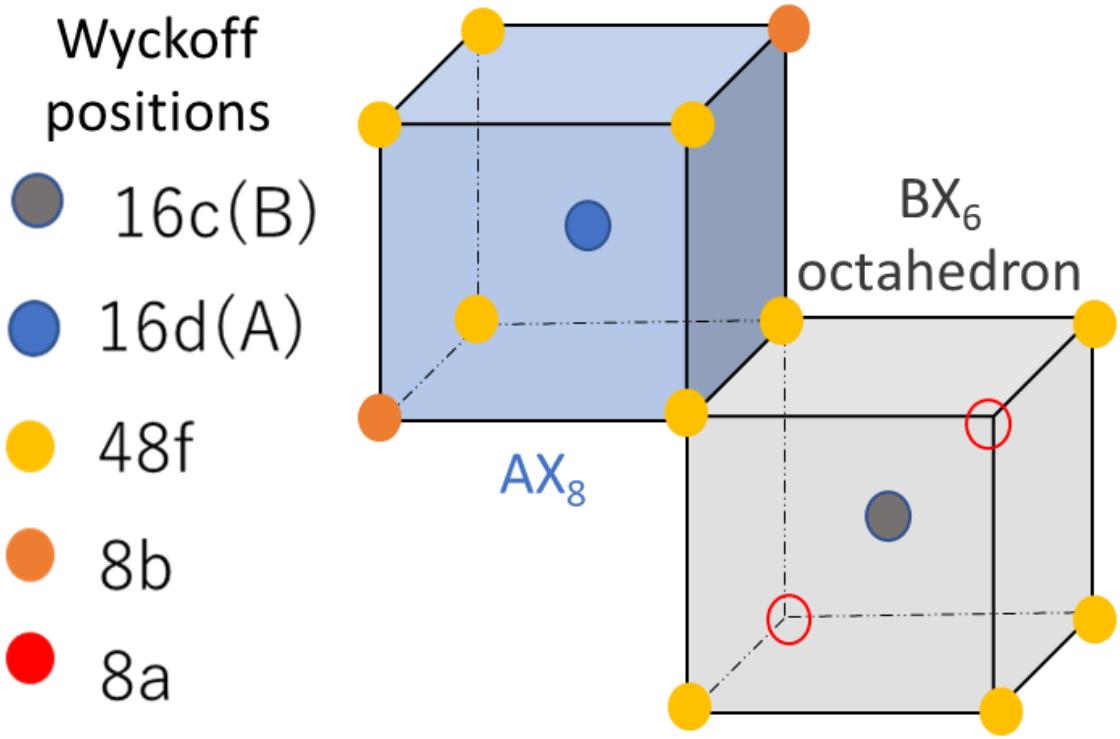

Fig. 3.14 Schematic of the pyrochlore-type structure. A and B cations occupy the 16d site (eight-coordinate site) and 16c site (six-coordinate site), respectively. X anions occupy the 48f and 8b sites, while the 8a site is unoccupied.

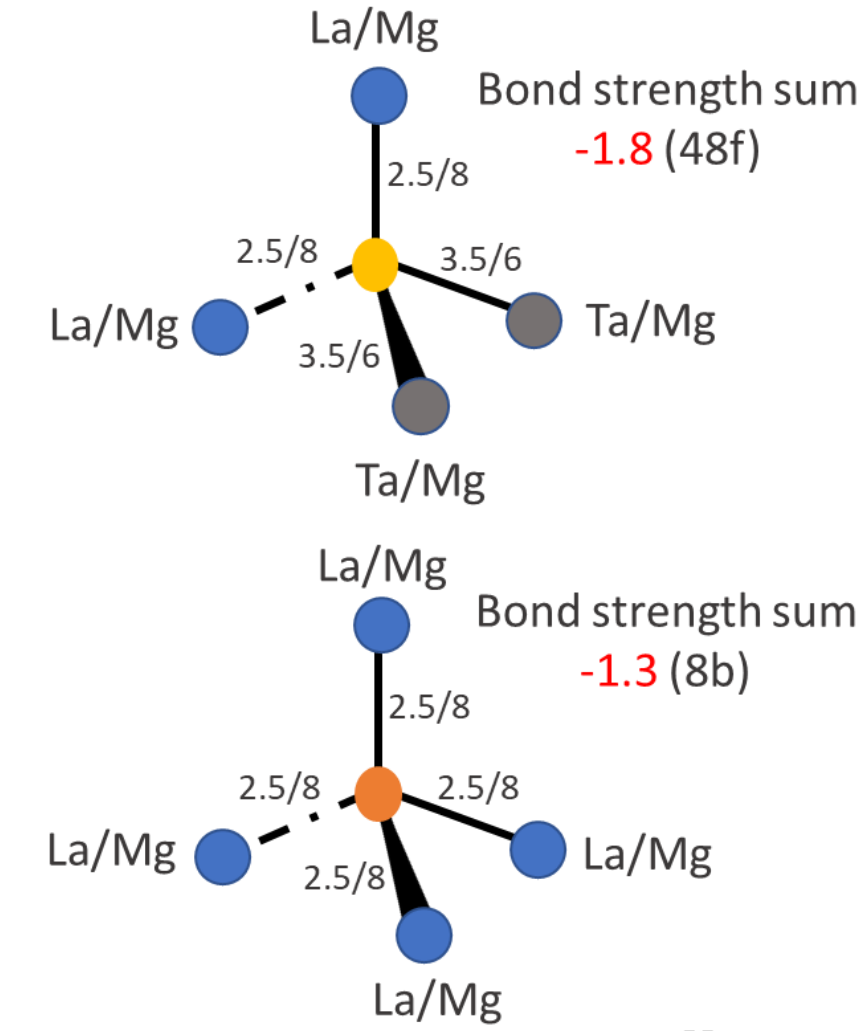

$$\text{(Bond strength sum)} = -\sum_i \frac{V_i}{n_i}$$

V_i : Valence of cation

n_i : Coordination number of cation

Fig. 3.15 Sum of the bond strengths of 48f and 8b site in Mg_2LaTaO_6. It is defined by the following equation: $-\sum_i \frac{V_i}{n_i}$, where V_i and n_i are the valence and coordination number of cation, respectively.

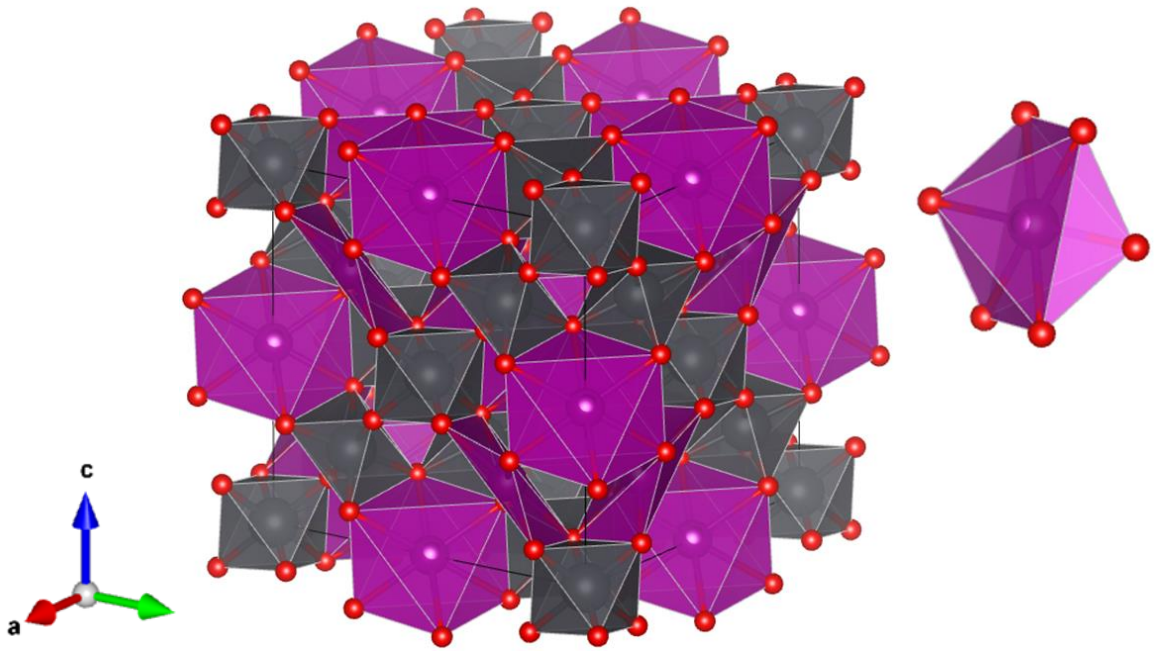

Fig. 3.16 Crystal structure of Pb_2MnReO_6 drawn using VESTA [29]. The BO_6 octahedron is highly distorted. The purple, black, and red spheres represent Mn/Re, Pb, and O, respectively. Mn^{2+} and Re^{6+} are disordered at 16c sites (purple polyhedral site).

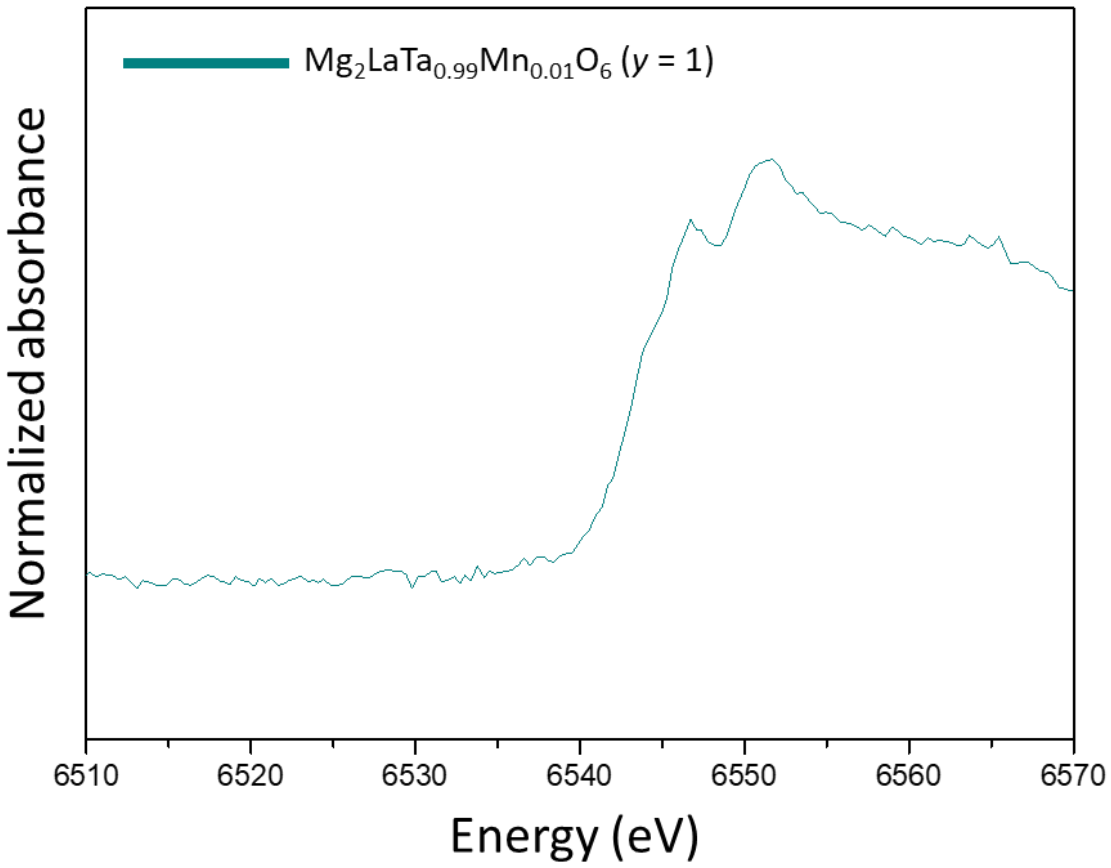

Fig. 3.17 Mn-K edge normalized XANES spectra of $Mg_2LaTa_{0.99}Mn_{0.01}O_6$ phosphors.

Table 3.1 Emission wavelength and coordination number of Mn^{2+}-activated oxide phosphors.

Host	Coordination number	Emission wavelength (nm)	Ref.
$CdAl_2O_4$	4	495	[34]
$KAlSi_2O_6$	4	513	[36]
Na_2ZnSiO_4	4	515	[31]
$SrAl_2Si_2O_8$	4	517	[40]
Na_2MgGeO_4	4	521	[35]
Zn_2SnO_4	4	523	[33]
Zn_2SiO_4	4	530	[30]
Mg_2LaTaO_6	6	540	This study
$CdSiO_3$	6	575	[37]
$Na_2Mg_2Si_6O_{15}$	6	630	[39]
$KMgBO_3$	6	636	[32]
$MgGeO_3$	6	680	[38]

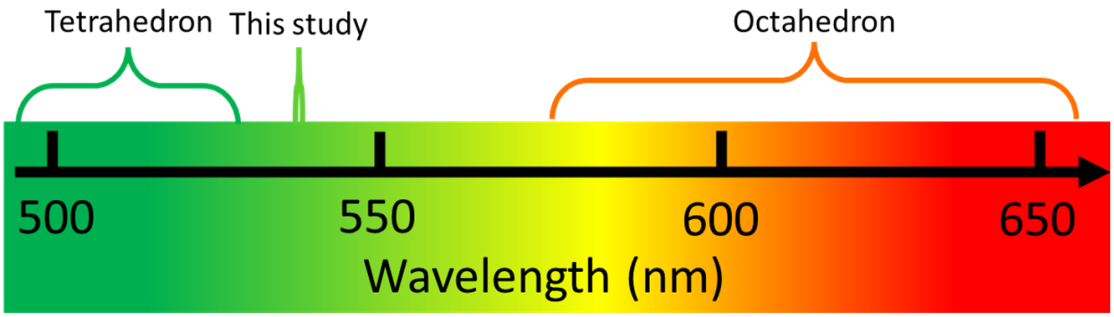

References

[1] E.F. Schubert, J.K. Kim, *Science* **308** (2005) 1274–1278.

[2] C.J. Humphreys, *MRS Bull.* **33** (2008) 459–470.

[3] C.C. Lin, R.S. Liu, *J. Phys. Chem. Lett.* **2** (2011) 1268–1277.

[4] S. Nakamura, T. Mukai, M. Senoh, *Appl. Phys. Lett.* **64** (1994) 1687–1689.

[5] Z. Xia, A. Meijerink, *Chem. Soc. Rev.* **46** (2017) 275–299.

[6] Z. Xia, Q. Liu, *Prog. Mater. Sci.* **84** (2016) 59–117.

[7] Y. Zhang, L. Luo, Guantong Chen, Y. Liu, R. Liu, X. Chen, *J. Rare Earths* **38** (2020) 1–12.

[8] K. Uheda, N. Hirosaki, H. Yamamoto, *Phys. Stat. Sol.* **(A) 203** (2006) 2712–2717.

[9] Y.Q. Li, J.E.J. van Steen, J.W.H. van Krevel, G. Botty, A.C.A. Delsing, F.J. DiSalvo, G. de With, H.T. Hintzen, *J. Alloys Compd.* **417** (2006) 273–279.

[10] X. Huang, J. Liang, B. Li, L. Sun, J. Lin, *Opt. Lett.* **43** (2018) 3305–3308.

[11] K. Li, J. Du, D. Poelman, H. Vrielinck, D. Mara, R. Van Deun, *ACS Mater. Lett.* **2** (2020) 771–778.

[12] L. Fu, Y. Yang, Y. Zhang, X. Ren, Y. Zhu, J. Zhu, Y. Wu, J. Wang, X. Feng, *J. Lumin.* **237** (2021) 118165.

[13] H. Kato, Y. Takeda, M. Kobayashi, H. Kobayashi, M. Kakihana, *Front. Chem.* **6** (2018) 467.

[14] D. Chen, Y. Zhou, Jiasong Zhong, *RSC Adv.* **6** (2016) 86285–86296.

[15] Laporte, W.F. Meggers, *J. Opt. Soc. Am.* **11** (1925) 459–463.

[16] D.D. Khalyavin, A.M.R. Senos, P.Q. Mantas, D.N. Argyriou, I. Tarroso Gomes, L.G. Vieira, J.L. Ribeiro, *J. Solid State Chem.* **180** (2007) 41–48.

[17] A. Belous, E. Pashkova, O. Gavrilenko, O. V'yunov, L. Kovalenko, *Ionics* **9** (2003) 21–27.

[18] L. Shi, Y. Han, S. Wang, J. Jiao, S. Chang, Z. Mu, Z. Mao, D. Wang, Z. Zhang, X. Lu, *J. Mater. Sci.: Mater. Electron.* **31** (2020) 4677–4686.

[19] C. Zhou, Y. Zhang, J. Zhu, X. Ren, Y. Zhu, P. Yin, L. Zhao, J. Wang, X. Feng, Spectrochim. *Acta, Part A* **268** (2022) 120655.

[20] R.D. Shannon, *Acta Cryst. A* **32** (1976) 751–767.

[21] S. Senthil Kumar, K.V.O. Nair, J. James, *J. Solid State Chem.* **177** (2004) 3873–3878.

[22] T. Senden, F. T.H. Broers, A. Meijerink, *Opt. Mater.* **60** (2016) 431-437.

[23] Y.-I. Kim, P.M. Woodward, *J. Solid State Chem.* **180** (2007) 2798–2807.

[24] T. Yamamoto, *X-ray Spectrom.* **37** (2008) 572-584.

[25] F. Farges, *Phys. Rev. B.* **71** (2005) 155109.

[26] A. Jerez, M.L. Lopez, S. Garcia-Martin, M.L. Veiga, C. Pico, *J. Mater. Sci.* **26** (1991) 5163–5166.
[27] L. Pauling, *J. Am. Chem. Soc.* **51** (1929) 1010–1026.
[28] K. Ramesha, L. Sebastian, B. Eichhorn, J. Gopalakrishnan, *Chem. Mater.* **15** (2003) 668–674.
[29] K. Momma, F. Izumi, *J. Appl. Crystallogr.* **44** (2011) 1272–1276.
[30] K.W. Park, H.S. Lim, S.W. Park, G. Deressa, J.S. Kim, *Chem. Phys. Lett.* **636** (2015) 141–145.
[31] Y. Wei, X. Han, E. Song, Q. Zhang, *Mater. Res. Bull.* **113** (2019) 90–96.
[32] L. Wu, B. Wang, Y. Zhang, L. Li, H.R. Wang, H. Yi, Y.F. Kong, J.J. Xu, *Dalton Trans.* **43** (2014) 13845–13851.
[33] L.T.T. Vien, N. Tu, D.X. Viet, D.D. Anh, D.H. Nguyen, P.T. Huy, *J. Lumin.* **227** (2020) 117522.
[34] W. Ran, L. Wang, Q. Liu, G. Liu, D. Qu, X. Pan, J. Shi, *RSC Adv.* (2017) 17612–17619.
[35] L. Hu, Q. Wang, X. Wang, Y. Li, Y. Wang, X. Peng, *RSC Adv.* **5** (2015) 104708–104714.
[36] X. Ding, G. Zhu, Q. Wang, Y. Wang, the *RSC Adv.* **5** (2015) 30001–30004.
[37] B. Lei, Y. Liu, Z. Ye, C. Shi, *J. Lumin.* **109** (2004) 215–219.
[38] G. Doke, A. Antuzevics, G. Krieke, A. Kalnina, M. Springis, A. Sarakovskis, *J. Lumin.* **234** (2021) 117995.
[39] W. Gong, J. Luo, W. Zhou, J. Fan, Z. Sun, S. Zeng, H. Pan, Z. Zhu, X. Yang, Z. Yu, X. Zhang, *J. Lumin.* **239** (2021) 118372.
[40] B. Wang, Y. Kong, Z. Chen, X. Li, S. Wang, Q. Zeng, *Opt. Mater.* **99** (2020) 109535.

Chapter 4

Conclusion

4.1 Garnet-type $Ca_2EuZr_{2-x}Sn_xGa_3O_{12}$ (x = 0, 0.5, 1, 1.5, and 2) red phosphors

Novel garnet-type $Ca_2EuZr_{2-x}Sn_xGa_3O_{12}$ (x = 0, 0.5, 1, 1.5, and 2) red phosphors were synthesized via a solid-state reaction to supplement the red component of white LEDs. XRD analysis revealed that the garnet-type structure was formed in all samples. In samples with x = 0 and 2, the diffraction peaks were shifted to higher angles owing to the lattice shrinking due to differences in ionic radius. The diffraction peaks of the samples with x = 0.5, 1, and 1.5 were broad, indicating that the formation of solid solutions was difficult. The results of Rietveld analysis showed that Zr^{4+} occupied only the octahedral site and Ga^{3+} occupied only the tetrahedral site in the garnet-type $Ca_2EuZr_2Ga_3O_{12}$ phosphor, whereas both Sn^{4+} and Ga^{3+} occupied the octahedral site and the tetrahedral sites in the garnet-type $Ca_2EuSn_2Ga_3O_{12}$ phosphor. The results of photoluminescence measurements indicated that the Ω_2/Ω_4 ratio decreased gradually with an increase in x. This is because the substitution of Sn^{4+} increased the length of the shared edge of the tetrahedron and dodecahedron and resulted in a change in the symmetry of the dodecahedron occupied by Eu^{3+}, which approached a square antiprism-like polyhedron.

4.2 Perovskite-type Mn^{4+}-activated $La_{5/3}MgTaO_6$ red phosphor and pyrochlore-type Mn^{2+}-activated Mg_2LaTaO_6 green phosphor

Cost-effective red-emitting phosphors with structures of $La_{5/3-(2/3)x}Ba_xMgTa_{0.99}Mn_{0.01}O_6$ (x = 0, 0.2, 0.4, 0.6, 0.8, and 1) and $La_{5/3-(2/3)y}Mg_{1+y}Ta_{0.99}Mn_{0.01}O_6$ (y = 0, 0.2, 0.4, 0.6, 0.8, and 1) were synthesized by a solid-state reaction for use in high-color-rendering white LEDs. An investigation of the luminescence properties of Mn-activated $La_{5/3-(2/3)x}Ba_xMgTa_{0.99}Mn_{0.01}O_6$ (x = 0, 0.2, 0.4, 0.6, 0.8, and 1) phosphors suggests that the absorption and emission of Mn^{4+} in perovskite-type $La_{5/3}MgTaO_6$ is related to the A-site deficiency of the structure. The deficiency of La^{3+} in $La_{5/3}MgTaO_6$ causes Mn^{4+} to occupy distorted six-coordinate octahedral sites, thereby relaxing the forbidden transition. The XANES spectra showed evidence that Mn^{4+} was located at the non-inversion center in the A-site deficient perovskite-type structure. The Mn^{4+}-activated $La_{5/3}MgTaO_6$ phosphor exhibits red emission under UV excitation at 365 nm, and thus has potential applications as a red phosphor in high-color-rendering white LEDs.

Similarly, the pyrochlore-type Mg_2LaTaO_6 phosphor exhibited green emission at ~540 nm under UV excitation at 254 nm. In conjunction with the crystallographic data of Mg_2LaTaO_6, this result suggests that Mn^{2+} is present in the six-coordinated octahedral sites with a center of inversion in Mg_2LaTaO_6. Our results suggest that the highly distorted BO_6 octahedron may weaken the crystal field, thereby resulting in green emission, and explaining the fact that Mn-activated Mg_2LaTaO_6 phosphor exhibited green emission despite the occupation of the six-coordinate sites.

謝辞

本研究を遂行するにあたり、お世話になった方々への感謝の気持ちを申し上げます。
森賀 俊広 教授には、数々の助言をいただき、研究を進めていく上で自分の知見や考え方を深めるきっかけを数多く頂きました。さらに、台湾とイスラエルでの留学の機会をいただき、3 年間の博士後期課程をとても有意義に過ごすことが出来ました。化学 C1 講座で得られた経験や研究の進め方は、今後の研究者人生において自分の大きな基盤になると思います。

村井 啓一郎 准教授には、学部から博士前期課程において指導教員として指導して頂きました。自分の行った研究に対してたくさんの意見を与えてくださり、いただいた意見に対して考察し、また実験を繰り返すという日々を送ってきて、自分で研究を進める力を養うことが出来ました。

同研究室の博士後期課程 1 年尾上 知也 様、前川 泰輝 様をはじめ、研究室の先輩方、後輩達には研究面や生活面でサポートしていただきました。

留学先である国立台湾科技大学の Shao-Ju Shih 教授、Henni Setia Ningsih 様にはダブルディグリー取得のため研究を指導して頂きました。安澤 幹人 教授、コインカー・パンカジ・マドウカー 准教授、浅田 沢 様には台湾留学の支援をして頂きました。テクニオン・イスラエル工科大学の Yehonadav Bekenstein 先生、Shai Levy 様には研究と生活面でサポート頂きました。福井 清 副学長、曽我部 孝行 様、そして日亜化学工業株式会社 様にはテクニオン・イスラエル工科大学派遣の支援をして頂きました。

最後に、徳島大学での 9 年間の生活を支えていただいた家族に感謝するとともに、協力していただいた皆様へ心から感謝の気持ちとお礼を申し上げたく、謝辞とさせていただきます。